Bioactive Materials 13 (2022) 223–238

Contents lists available at ScienceDirect

Bioactive Materials

journal homepage: www.keaipublishing.com/en/journals/bioactive-materials

Blockading a new NSCLC immunosuppressive target by pluripotent autologous tumor vaccines magnifies sequential immunotherapy

Hong Wu [a,1], Hongyan Li [b,1], Yiqiang Liu [a,1], Jingchen Liang [a], Qianshi Liu [a], Zhigang Xu [c], Zhongzhu Chen [c], Xia Zhang [d], Kun Zhang [b,*], Chuan Xu [a,**]

[a] Integrative Cancer Center & Cancer Clinical Research Center, Sichuan Cancer Hospital & Institute, Sichuan Cancer Center School of Medicine, University of Electronic Science and Technology of China, No.55, Section 4, South Ren-min Road, Chengdu, 610042, Sichuan, PR China
[b] Department of Medical Ultrasound and Central Laboratory, Shanghai Tenth People's Hospital, Ultrasound Research and Education Institute, Tongji University School of Medicine, No. 301 Yan-chang-zhong Road, Shanghai, 200072, PR China
[c] International Academy of Targeted Therapeutics and Innovation, Chongqing University of Arts and Sciences, NO. 319, Red River Avenue, Yong-chuan, 402160, Chongqing, PR China
[d] Institute of Pathology and Southwest Cancer Center, Southwest Hospital, Third Military Medical University (Army Medical University), NO. 30, Gao-tan-yan-zheng Street, Chongqing, 400038, PR China

ARTICLE INFO

Keywords:
Autologous tumor vaccines (ATVs)
Sequential immunotherapy
Immunosuppressive microenvironment
Tumor tropism
Immune escape target

ABSTRACT

The presence of multiple immunosuppressive targets and insufficient activation and infiltration of cytotoxic T lymphocytes (CTLs) allow tumor cells to escape immune surveillance and disable anti-PD-1/PD-L1 immunotherapy. Nanobiotechnology-engineered autologous tumor vaccines (ATVs) that were camouflaged by tumor cell membrane (TCM) were designed to activate and facilitate CTLs infiltration for killing the unprotected lung tumor cells, consequently realizing the sequential immunotherapy. PDE5 was firstly screened out as a new immunosuppressive target of lung cancer in clinical practice. Immediately afterwards, phosphodiesterase-5 (PDE5) and programmed cell death 1 ligand 1 (PD-L1) dual-target co-inhibition was proposed to unfreeze the immunosuppressive microenvironment of NSCLC. Systematic studies validated that this ATVs-unlocked sequential immunotherapy after co-encapsulating PDE5 inhibitor and NO donor (*i.e.*, L-arginine) exerted robust anti-tumor effects through increasing inducible nitric oxide synthase (iNOS) expression, blockading PDE5 pathway and activating systematic immune responses, which synergistically eradicated local and abscopal lung cancers in either orthotopic or subcutaneous models. The pluripotent ATVs that enable PDE5 inhibition and sequential immunotherapy provide a new avenue to mitigate immunosuppressive microenvironment and magnify anti-PD-1/PD-L1 immunotherapy.

1. Introduction

Immune escape-represented immunosuppressive microenvironment is still the dominant limiting factor that disables most immunotherapeutic means in fundamental or clinical cases [1–3]. As a paradigm, programmed cell death 1 ligand 1 (PD-L1) that is highly-expressed in tumor cells, usually acts as an immunosuppressive target to prevent tumor cells from the recognition by activated effector T cells [4–6]. This immune escape behavior severely impaired T cells-based anti-tumor strategy [1]. Recently, many endeavors have been made in anti-PD-1/PD-L1 immunotherapy, and the pioneering work was awarded with the 2018 Nobel Prize [7–12]. Despite receiving considerably-increased interests, only a small fraction of patients was benefited from anti-PD-1/PD-L1 immunotherapy even in the presence of highly-expressed PD-L1 [13–15]. Such disappointing outcomes are probably attributed to two aspects, (i) inadequate activation and rare infiltration of cytotoxic T lymphocytes (CTLs) cause insufficient armed CTLs to enter tumor and execute killing effect towards tumor cells [15–17]; and (ii) Even though the cold tumor is switched into hot ones, the presence of some other immunosuppressive targets (*e.g.*, CTLA-4,

Peer review under responsibility of KeAi Communications Co., Ltd.
* Corresponding author.
** Corresponding author.
E-mail addresses: zhang1986kun@126.com (K. Zhang), xuchuan100@163.com (C. Xu).
[1] The authors contributed equally to this work.

https://doi.org/10.1016/j.bioactmat.2021.10.048
Received 29 August 2021; Received in revised form 19 October 2021; Accepted 30 October 2021
Available online 3 November 2021

Siglec-15, TREM2, CD24, Ptpn2, CD47) make tumor cells camouflaged, featured of immune escape [5,18–22]. Unfortunately, the two concerns have not been simultaneously addressed yet. On this account, new solution to concurrently address the two concerns for realizing sequential immunotherapy is desirable.

In this report, phosphodiesterase-5 (PDE5) was firstly screened out as a new immunosuppressive target since it was demonstrated to be highly-expressed in lung adenocarcinoma tissues of patients and its expression level negatively associated with the prognosis of lung adenocarcinoma. Inspired by it, two immunosuppressive targets (*i.e.*, PDE5 and PD-L1) co-inhibition strategy was established to maximally improve immunotherapeutic outcomes and inhibit lung tumorigenesis, which could address the aforementioned 2nd concern that single anti-PD-1/PD-L1 immunotherapy encounter (Step ④ in Scheme 1). Herein, the classic PDE5 inhibitor (PDE5i) that has been widely used to treat erectile dysfunction (ED) and pulmonary arterial hypertension *via* slowing intracellular cGMP degradation to increase endogenous nitric oxide release [23,24], was used to blockade PDE5 immunosuppressive target in lung cancer. Systematic experiments validated that PDE5i indeed inhibited lung cancer *in vitro* and *in vivo* through activating the systematic anti-tumor immune responses especially after combing with PD-L1 immune checkpoint blockade.

In an attempt to address the 1st concern, autologous tumor vaccines (ATVs) were developed after camouflaging mesoporous organosilica nanoparticle (Mon) carrier with the tumor cell membrane (TCM) because TCM held abundant antigens [25]. The exposed antigens on TCM shell could promote the nanobiotechnology-engineered ATVs to be engulfed by dendritic cells (DCs) and directly result in pro-inflammatory signal activation and DCs maturation, and further boost activation and infiltration of CTLs (Steps ①-③ in Scheme 1). As well, the TCM-driven tumor tropism specifically allowed more pluripotent ATVs to enter lung cancer for inhibiting tumor, addressing the non-specificity of previous ligands chelation-mediated active targeting or leukocytes phagocytosis-mediated accumulation [26]. Noticeably, before TCM camouflaging, PDE5i and nitrogen donor (*i.e.*, L-arginine (LA)) were co-encapsulated in Mons of ATVs to improve specific delivery of PDE5i and supply NO for further enhancing PDE5i efficacy and mitigating immunosuppressive microenvironment. Inspiringly, the pluripotent ATVs sequentially addressed the 1st concern and the 2nd concern that anti-PD-L1/PD-1 immunotherapy suffered from, which, thereby, established a sequential immunotherapy strategy (Steps ①-④). The ATVs-unlocked sequential immunotherapy boosted systematic immune responses associated with increased DC maturation and $IFN\gamma^{+}CD8^{+}$ T cell population and more inflammatory cytokine secretion (Step ⑦ in Scheme 1), consequently harvesting significantly-enhanced anti-tumor and anti-metastasis outcomes *in vivo* through direct immune-mediated tumoricidal effect and immunosuppressive microenvironment regulation. Especially when combining with PD-L1 blockading, this distinctive ATVs considerably enhanced the therapeutic consequences of orthotopic and subcutaneous lung cancers and eradicated local and abscopal lung tumors (Steps ④-⑥ in Scheme 1). Taken all above together, clinically-screened and experientially-validated PDE5 indeed can

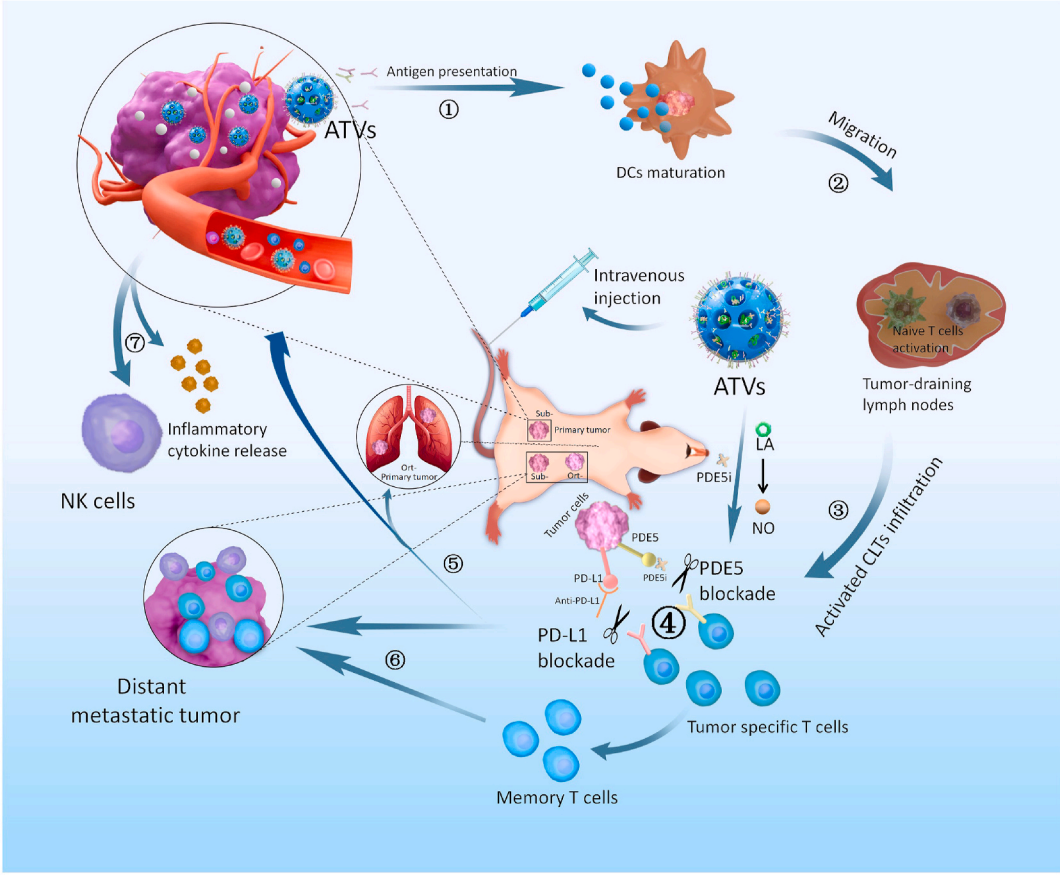

Scheme 1. Mechanistic schematic on how LA and PDE5 co-loaded pluripotent ATVs enable the sequential immunotherapy against primary and distant lung tumors in either orthotopic (Ort-) or subcutaneous (Sub-) models. In detail, Step ① represents engulfment and presentation of antigens on ATVs by DCs and DC maturation; Step ② represents the migration of matured DCs to tumor-draining lymph nodes and CTLs activation; Step ③ indicates the infiltrations of activated CTLs into lung tumor; Step ④ indicates the PDE5 blockade by PDE5i in such ATVs, wherein LA release induced NO production to benefit PDE5i efficacy, and anti-PD-L1 also blockaded PD-L1 immunosuppressive target to constitute the PDE5/PD-L1 dual-target co-inhibition strategy; Steps ⑤ and ⑥ mean the inhibition actions of activated systematic responses against primary (⑤) and distant metastatic (⑥) tumors, respectively; and Step ⑦ represents secretions of some pro-inflammatory cytokines.

behave as an immunosuppressive target in lung cancer, which can also act as a reliable drug target of lung cancer. More significantly, the established pluripotent ATVs and the ATVs-enabled unprecedented sequential immunotherapy can maximally exert the anti-tumor immune efficacy and open up a new direction for immunotherapy, and both of which hold great potential in clinical translation.

2. Results and discussion

2.1. Screening PDE5 as an immunosuppressive target in clinical practice and in PDE5 inhibition-based lung cancer repression tests

To determine whether PDE5 can act as the immunosuppressive target of NSCLC, PDE5 protein abundances in five NSCLC cell lines including LLC, A549, H1975, H1299 and H358 were firstly monitored comparing to those in lung bronchial epithelial cells (*i.e.*, HBE). As expected, PDE5 levels in all tested cancer cell lines are found much higher than that in HBE cells (Fig. 1a). Consistent with *in vitro* results, more PDE5 proteins are expressed in cancer tissues as compared with normal tissues (Fig. 1b). Subsequently, we explored the correlation between aberrant PDE5 expression and the prognosis of NSCLC patients. Immunohistochemical (IHC) analysis of PDE5 expression in tissue samples from 81 patients indicates that 63% patients exhibit higher PDE5 expression in tumor tissues (Fig. 1c and d). Moreover, Kaplan-Meier analysis shows that high PDE5 expression correlates with poor overall survival (OS), whereas low PDE5 expression gives birth to favorable clinical outcomes (Fig. 1e). In colony formation assay, PDE5i lowers the colony formation efficiency of A549 and Lewis lung cancer (LLC) cells (Fig. 1f). Subsequently, *in vivo* anti-tumor assessment on LLC-bearing C57/BL6 using PDE5i indicates that PDE5i alone exerts a potent therapeutic effect (Fig. 1g and h), where the weight and volume of tumors in PDE5i-treated group are decreased (Fig. 1i and j). To unravel the underlying principle of PDE5i-enhanced anti-tumor outcomes, we examined the maturation degree of antigen-presenting cells (APCs) such as DCs. It is found that PDE5i treatment remarkably elevated the percentages of co-stimulatory molecules CD80/CD86 that are usually regarded as the representative markers for DC maturation in peripheral blood and tumor tissues (Fig. 1k,l). Moreover, it also brings about more upregulations of $CD8^+$ and $CD4^+$ T cells in PDE5i-treated peripheral blood mononuclear cells (PBMCs) and concurrently facilitates $CD8^+$ T

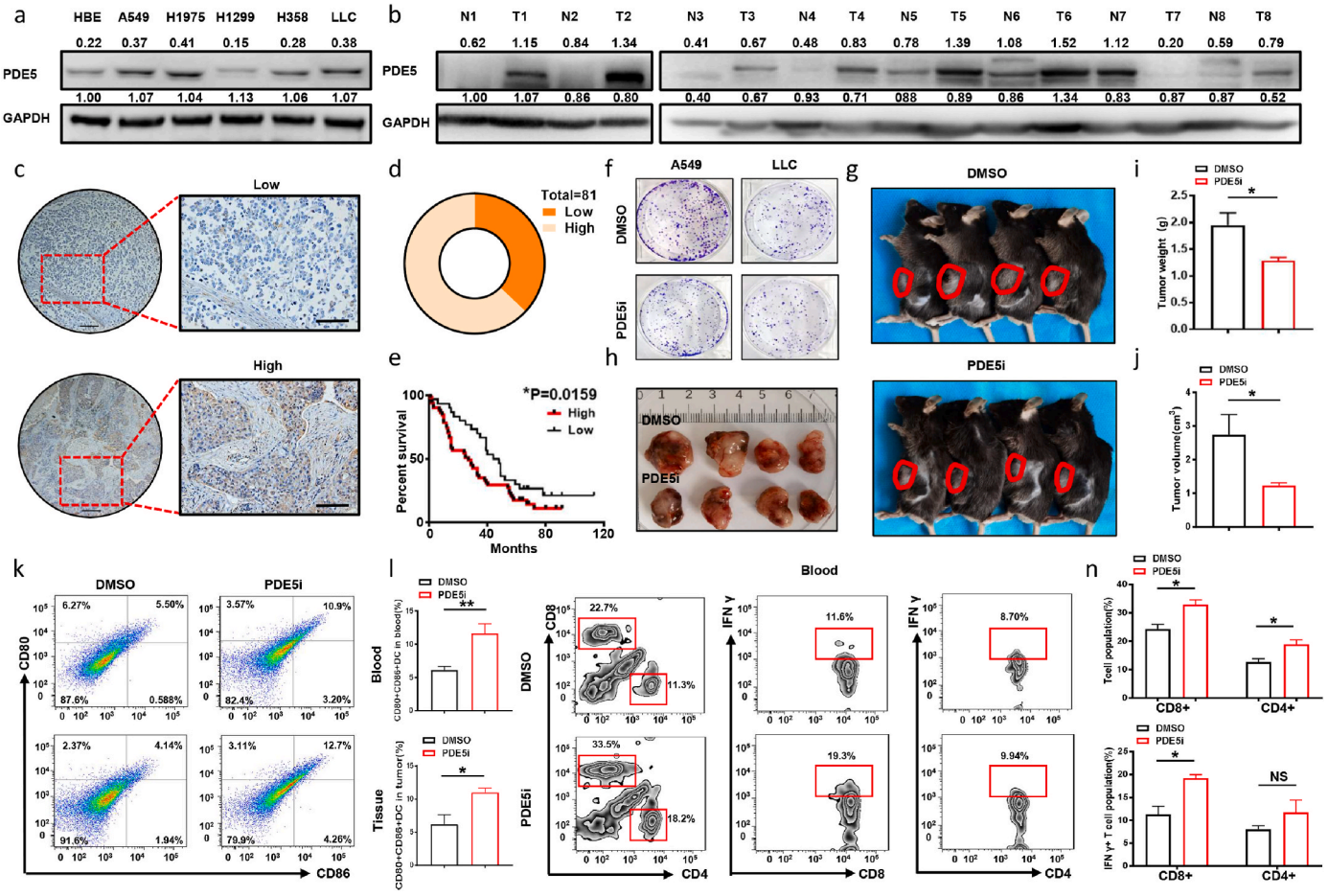

Fig. 1. Screening PDE5 as the immunosuppressive target of NSCLC. (a) Immunoblotting patterns of PDE5 protein in various LAC cells and HBE cells; (b) Immunoblot analysis of PDE5 protein abundances in the paired LAC tumor tissue (T) and adjacent normal ones (N) harvested from eight LAC patients; (c) Representative immunohistochemical images of tumors harvested from LAC patients with $PDE5^{low}$ and $PDE5^{high}$ expression, scale bar: 50 μm (left), 100 μm (right); (d) Quantitative analysis of PDE5 expression in 81 cases of LAC tumor tissues. (e) Kaplan–Meier analysis of the survivals of LAC patients with $PDE5^{low}$ and $PDE5^{high}$; (f) *In vitro* colony formation assay of A549 and LLC that were treated with DMSO or PDE5i (10 μM) for 5 days; (g–j) LLC xenografted tumors in male C57/BL6 mice treated with DMSO or PDE5i (*i.v.* PDE5i 100 mg/kg per day for 5days) after the tumor reached 25–50 mm^3. The macroscopic mice images (g) and tumor images (h), tumor weight (i) and tumor volume (j) were acquired on day 28 after inoculation; (k,l) FCM patterns (k) and quantitative statistics (l) for determining DC maturation after staining with CD80 and CD86, DCs were harvested from the peripheral blood mononuclear cells (upper) and tumor tissues (bottom) of tumor-bearing mice treated with PDE5i or DMSO (control). (m,n) Representative FCM plots (m) and quantitative data (n) for distinguishing the subtypes in PBMCs, including $CD8^+$ T cells ($CD45^+CD8^+$), $CD4^+$ T cells ($CD45^+CD4^+$), $CD8^+IFN\gamma^+$ ($CD45^+CD8^+IFN\gamma^+$) T cells and $CD4^+IFN\gamma^+$ ($CD45^+CD4^+IFN\gamma^+$) T cells in the tumor-bearing mice treated with PDE5i or DMSO. The data are presented as the mean ± standard deviation (SD) (n = 4). 'NS' means no significance, $^*P < 0.05$, and $^{**}P < 0.01$.

cells to secrete more IFNγ (Figure 1m,n). Considering the excellence of nanotechnology in promoting drug delivery, we loaded PDE5i to Mon carrier (Mon@PDE5i). Of note, Mon@PDE5i performs much better in delaying tumor growth than free PDE5i (Figs. S1a and b). Together, these results sufficiently suggest that PDE5 is an immunosuppressive target of NSCLC, and blockading this target with PDE5i holds great potential in directly exerting cytotoxic effects and anti-tumor immune responses against NSCLC.

2.2. Preparation of this pluripotent ATVs (Mon@LA-PDE5i@M)

To address the non-specific delivery of PDE5i, drug delivery system (DDS)-represented nanobiotechnology was introduced to load PDE5i and yield ATVs. As illustrated in Fig. 2a, Mon carrier is adopted to load and deliver PDE5i along with LA (Mon@LA-PDE5i) [25], followed by intact TCM coating (Mon@LA-PDE5i@M) to obtain the pluripotent ATVs featuring tumor tropism, wherein another intermediate that only load PDE5i (Mon@PDE5i) is yielded. TCM coating that is clearly observed on Mon@LA-PDE5i@M enabled the uniform dispersity of Mon@LA-PDE5i@M ATVs (Fig. 2b). The elevations of particle size and zeta potential also validate the successful TCM coating (Fig. 2c–e). The complete retention of antigen activity on TCM is the prerequisite of realizing DCs-mediated cross-presentation, DCs maturation and effector T cell activation. Integrity analysis of protein ingredient using gel electrophoresis reveals that the membrane proteins within TCM are well retained and wrapped onto ATVs (Fig. 2f). Furthermore, immune blotting analysis demonstrates the successful protein extraction and coating without injures to the membrane and intracellular protein markers including plasma membrane-specific markers of E-cadherin and Na^+/K^+ ATPase. Inspiringly, this extraction process displays a high selective retention of membrane fragments since the intracellular protein markers of mitochondria, nucleus, and cytosol, *e.g.*, COX IV, Ki-67, β-actin, Lamin B1 and GAPDH, are poorly present on the cracked cancer cell membrane after protein extraction (Fig. 2g). *In vivo* fluorescence imaging results validate the higher accumulation of Mon@LA-PDE5i@M ATVs in lung and LLC tumors after *i.v.* administration compared with Mon@LA-PDE5i. Even after 48 h, massive ATVs remain enriched in tumors (Fig. 2h), which is also confirmed by quantitative analysis (Fig. 2i). With preserving the intact protein or antigen activity in such pluripotent ATVs, TCM-driven tumor tropism can be expected to promote the targeting delivery of PDE5i and LA-involved ATVs into NSCLC. The most phagocytosis of Mon@LA-PDE5i@M by A549 and LLC cells *in vitro* is also observed (Fig. 2j), and it receives the highest inhibition rate against A549 cells (Fig. S1c).

2.3. ATVs-unlocked sequential immunotherapy against NSCLC

In vivo antitumor studies also reflect that Mon@LA-PDE5i@M exerts the most robust suppression effect against LLC syngeneic tumors (Fig. 3a and b), harvesting the best antitumor consequences (Fig. 3c,e,f). The stable body weight indicates the excellent biosafety of Mon@LA-PDE5i@M (Fig. 3d). To figure out the anti-tumor mechanism of such special ATVs, we investigated how immune cells were trained by massive Mon@LA-PDE5i@M ATVs to attain such an appealing therapeutic effect. Flow cytometry (FCM) analysis reveals that Mon@LA-PDE5i@M treatment significantly promotes DC maturation ($CD80^+CD86^+$ DCs) in both tumor-draining lymph nodes (Fig. 3g and h) and tumors (Fig. 3i and j). The pro-inflammatory cytokines including IL12p70, TNF-α and IL-6 in the serum of LCC tumor bearing mice are also remarkably increased, which is favorable for triggering the anti-tumor immunological responses (Fig. 3k–m). As a result, the proportions of both $CD8^+$ and $CD4^+$ T cells in serum are tremendously increased in Mon@LA-PDE5i@M-treated group (Fig. 3n–p). These results confirm that such LA/PDE5i-co-loaded ATVs completed the sequential immunotherapy (Step ①-④) to suppress tumorigenesis, covering PDE5 blockade-enabled immunosuppressive microenvironment alleviation, simulated DCs maturation and armed CTLs infiltration.

2.4. A deep insight into LA/PDE5i co-loaded ATVs for activating systematic immune responses

To acquire a further insight into the underlying anti-tumor mechanisms of the pluripotent ATVs-activated immune responses, we made detailed, in-depth and comprehensive investigations. Firstly, we scrutinized the contribution of LA in Mon@LA-PDE5i@M to the activated systematic immune responses since LA as the endogenous NO donor could produce nitric oxide under inducible nitric oxide synthase (iNOS) to elevate anti-tumor cytotoxity and enhance immune responses [27]. Immunofluorescence (IF) staining shows that iNOS mainly resides in the cytoplasm and nuclei of A549 and LLC cancer cells (Fig. S2a). LA integration into Mon@LA-PDE5i ATVs significantly improves iNOS expression (Fig. 4a). In particular, TCM coating augments ATVs accumulation *via* tumor tropism and further favors iNOS expression in a time-dependent manner (Fig. 4a and b). Moreover, identical to immune-blot result, qRT-PCR analysis also suggests Mon@LA-PDE5i@M performs the best in boosting iNOS expression (Figs. S2b and c). Inspired by the highest iNOS expression, Mon@LA-PDE5i@M treatment receives the highest NO birth in both A549 and LLC cancer cells, as evidenced by both qualitative (Fig. 4c) and quantitative (Fig. 4d–g) results. Thereafter, it brings about the remarkably inhibited cell proliferation (Fig. 4h) and colony formation efficiency (Fig. 4j), and leads to the utmost apoptosis (Fig. 4k). Furthermore, the anti-tumor effect is impaired by NO scavenger (NO–S), as evidenced by cell proliferation test (Fig. 4i), clone formation assay (Fig. 4j) and apoptosis assay (Figure 4l), which indirectly demonstrates that Mon@LA-PDE5i@M can produce NO to kill tumor cells.

Subsequently, the influences of the LA/PDE5i co-loaded ATVs on DCs as the dominant APCs were surveyed. FCM results show that any PDE5i-involved nanoparticle treatment can increase DC maturation in comparison to Mon alone, while Mon@LA-PDE5i@M yields the highest proportion of matured DCs due to the autologous antigens on TCM shell (Figure 4m,n). Regarding this, the pluripotent ATVs treatment unexpectedly induces the tremendously increased secretions of pro-inflammatory cytokines (TNF-α, IL-6, and IL12p70), which even overweighs LPS stimulation (Fig. 4o–q). Consistent with DC maturation results, tumor-cell debris after Mon@LA-PDE5i@M treatment can also act as antigens to trigger the highest levels of DC-secreted immune cytokines, such as TNFα, IL-6 and IL-12p70, determining that such PDE5 inhibition-involved ATVs are much preferable for enhancing systematic immune responses (Fig. 4r–u). To reach an in-depth understanding of ATVs-activated immune responses, we supervised the expressions of related genes and proteins. In detail, Mon@LA-PDE5i@M ATVs are found to increase maturation-related gene expressions including Oas1b, Isg20, Irf7, Inos, Ifit2, Ifit1, Ifit44, Ifit203, Ddx58, IFNγ, Rsad2, and Oas11 in bone marrow-derived DCs (Fig. 5a).

We also inspected iNOS expression at both mRNA and protein levels and traced NO release. It is obtained that Mon@LA-PDE5i@M stimulation propels up-regulations of both iNOS expression (Fig. 5b and c) and NO release (Fig. 5d and e) in DCs. To uncover the hidden regulation pathway, the alterations of NF-κB and cGAS signaling after different treatments were monitored, because NF-κB and cGAS signaling are commonly pro-inflammatory signaling pathway and NF-κB is responsible for increasing the transcription of endothelial cell nitric oxide synthase (eNOS) in response to laminar shear stress [28]. Intriguingly, Mon@LA-PDE5i@M treatment significantly stimulates NF-κB and cGAS signaling activation, which is similar to LPS treatment (Fig. 5f). Once combining with NO–S, both NF-κB and cGAS signaling activations are significantly suppressed (Fig. 5g). These results adequately indicate that the LA-loaded ATVs can activate NF-κB and cGAS signaling pathways to induce aforementioned high iNOS expression and NO release, which will in return benefit PDE5i action in promoting DC maturation. As expected,

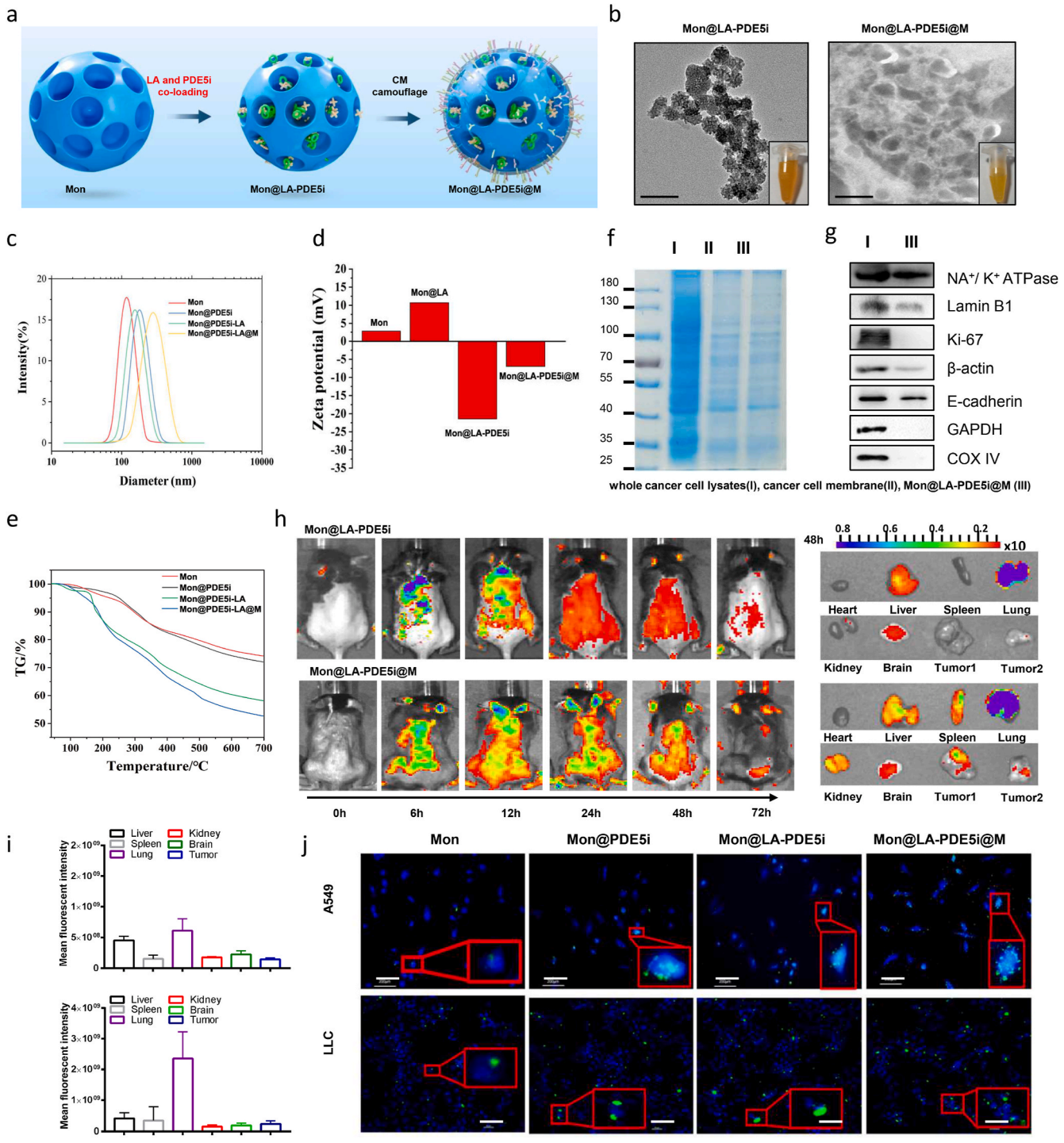

Fig. 2. Synthesis of this pluripotent ATVs (Mon@LA-PDE5i@M). (a) Schematic illustration of the synthesis procedures of Mon@LA-PDE5i@M; (b) TEM images of Mon@LA-PDE5i and Mon@LA-PDE5i@M, and scale bar: 100 nm; (c–e) The spherical shape (c) and average hydrodynamic size (d,e) of Mon@LA-PDE5i@M ATVs compared with other nanoparticles; (f) SDS-PAGE analysis of whole cancer cell lysates (I), cancer cell membrane (II), and Mon@LA-PDE5i@M ATVs (III) after staining with coomassie blue; (g) Immunoblotting analysis of whole cancer cell lysate (I) and Mon@LA-PDE5i@M ATVs (III) for determining plasma membrane-specific markers and intracellular protein markers. Samples were run at identical protein concentrations and then experienced immunostaining with membrane markers and intracellular markers; (h,i) *In vivo* fluorescence images of LLC tumor-bearing mice for studying the bio-distribution of ATVs after certain time points post-*i.v.* injection. Fluorescence images (h) and mean fluorescence intensity (i) of *ex vivo* tumors show the distributions of biomaterials in major organs after 48 h post-*i.v.* injection. The data are presented as the mean ± SD (n = 3) and the statistical significances are obtained using two tailed unpaired *t*-test. (j) LCSM images for monitoring the uptake of different samples by A549 and LLC cells, blue (DAPI), green (Mon, Mon@PDE5i, Mon@LA-PDE5i and Mon@LA-PDE5i@M ATVs), and scale bar: 200 μm.

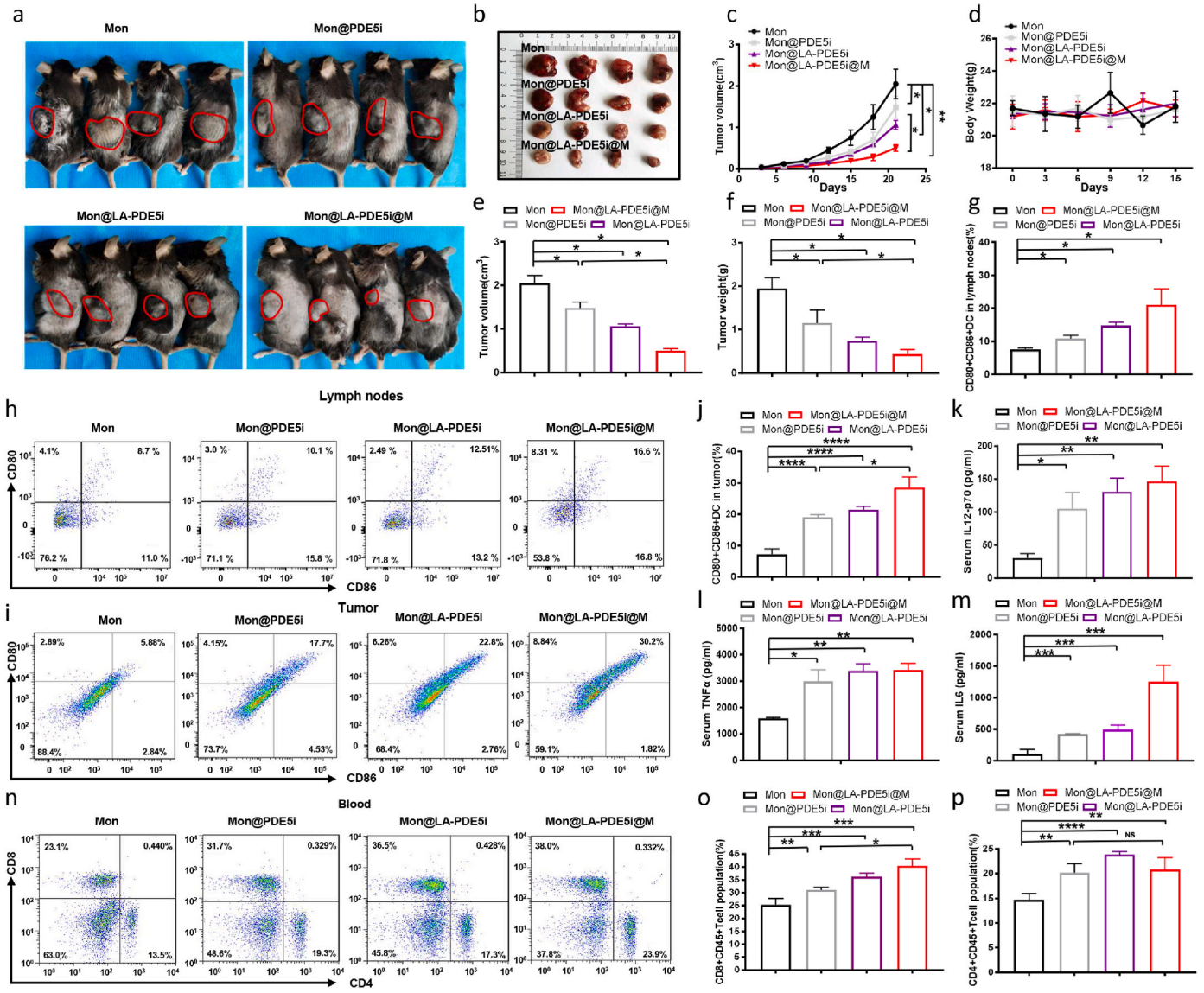

Fig. 3. ***In vivo*** **anti-tumor evaluation of pluripotent ATVs (Mon@LA-PDE5i@M)** ***via*** **activating systematic immune responses.** (a–f) Anti-tumor evaluations in tumor bearing male C57/BL6 mice treated with different samples including Mon, Mon@PDE5i, Mon@LA-PDE5i, Mon@LA-PDE5i@M ATVs (I.V. 100 mg/kg per day for 5 days). Macroscopic images of mice (a), harvested tumors (b), quantitative tumor volume (e) and tumor weight (f) were acquired on day 28 after inoculation. Time-dependent variation profiles of tumor volume (e) and mice body weight (d) were recorded; (g–j) FCM patterns (h,i) and quantitative data (g,j) of DC maturation ($CD80^+CD86^+$) in the tumor-draining lymph nodes and tumor tissues harvested from tumor-bearing mice on day 28 after inoculation; (k–m) Secretion levels of IL-12p70 (k), TNF-α (l) and IL-6 (m) in serum, and they were analyzed by ELISA after 5 days post-different treatments; (n–p) Representative FCM patterns (n) and quantitative data (o,p) for recognizing the subtypes in PBMCs including $CD8^+$ ($CD45^+CD8^+$) T cells (o), $CD4^+$ ($CD45^+CD4^+$) T cells (p) in the LLC tumor-bearing mice after various treatments. The data are presented as mean ± standard deviation (SD) (n = 4). 'NS' means no significance, $^*P < 0.05$, $^{**}P < 0.01$, $^{***}P < 0.001$ and $^{****}P < 0.0001$.

the elevated iNOS expression and NO release by such pluripotent ATVs promote DC maturation (Fig. 5h and i) and increase immune cytokine secretions including IL-6, IL12p70 and TNFα (Fig. 5j–l), while NO–S introduction lowers DC maturation and decreases cytokine secretions (Fig. 5h–l). These explicit results validate that LA can assist PDE5i in Mon@LA-PDE5i@M to reinforce immune responses especially in combination with tumor tropism-enhanced accumulation.

2.5. *Sequential immunotherapy enabled by pluripotent ATVs alone or plus anti-PD-L1 for suppressing primary tumors on subcutaneous model*

Despite realizing sequential immunotherapy, this single PDE5 target blockade by PDE5i&LA-loaded ATVs alone still fails to address other immunosuppressive targets-derived immune escape. Herein, co-inhibition of PDE5 and PD-L1 dual immunosuppressive targets is carried out on subcutaneous LLC xenograft tumor (Fig. 6a), which is expected to further potentiate the sequential immunotherapy. Besides LA-augmented NO production for direct anti-tumor, the tumor tropism-enhanced accumulation and NO & PDE5i-enhanced immune responses also take the responsibility for enabling Mon@LA-PDE5i@M ATVs to gain the inspiring inhibitory consequences (Fig. 6b–e). More significantly, once combining with anti-PD-L1 blockade, the largest delayed tumor growth is acquired. This phenomenon suggests that the co-inhibition strategy of dual immunosuppressive targets is preferable than single target blockade and thus merits chase for highly-efficient anti-tumor outcomes. In addition, no abnormal weight change and no evident pathological difference indicate the minimal systematic toxicity of ATVs (Fig. 6f and Fig. S3), guaranteeing high therapeutic biosafety of

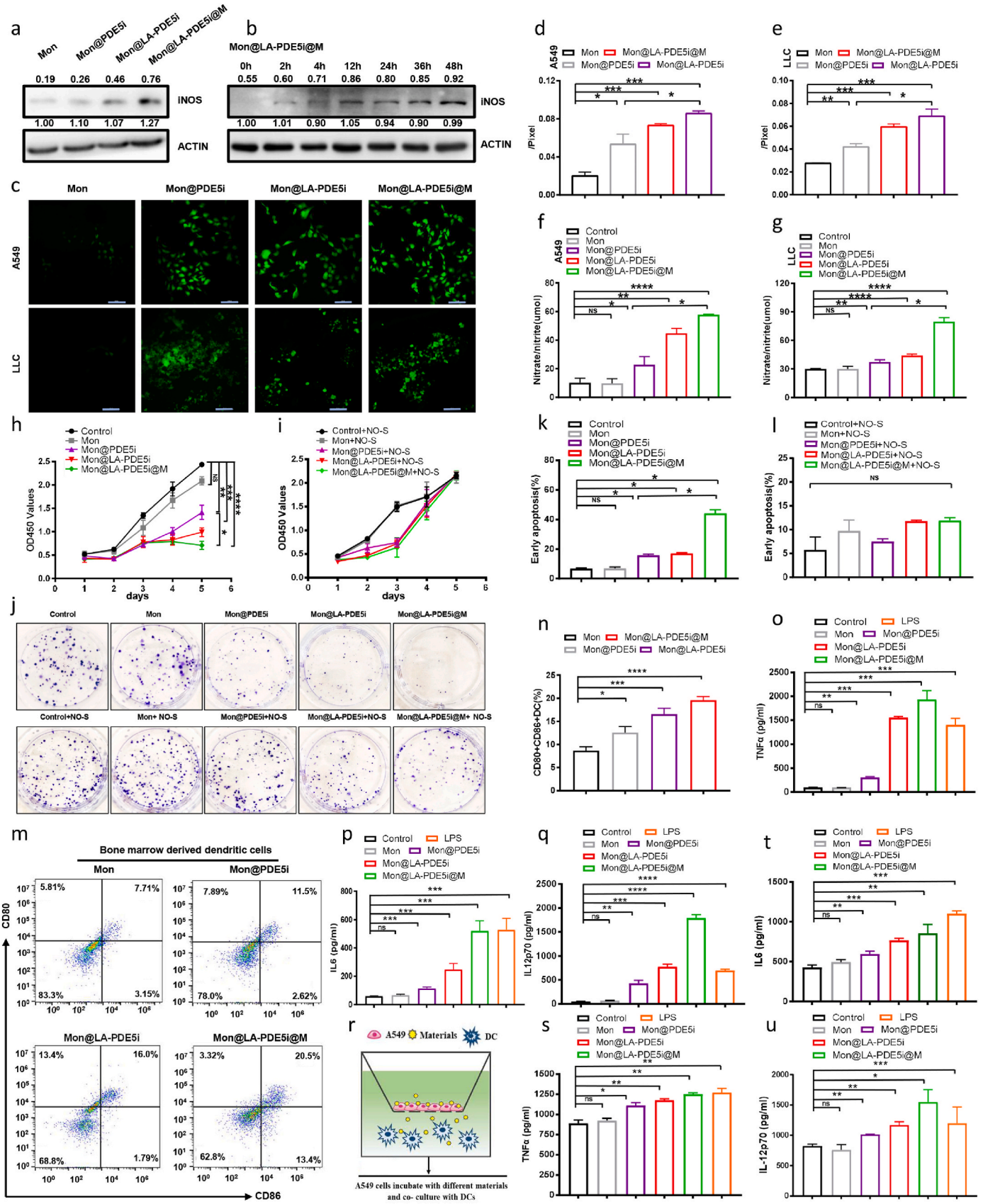

(caption on next page)

Fig. 4. *In vitro* systematic evaluations of Mon@LA-PDE5i@M ATVs-enabled sequential immunotherapy in activating systematic anti-tumor immune responses *via* LA-mediated NO release and ATVs-enhanced antigen capture by DCs. (a,b) Immunoblotting analysis of iNOS expression in A549 cells treated with different samples for 48 h (a) and with Mon@LA-PDE5i@M ATVs alone (b) at a fixed dosage of 0.5 mg/mL for varied time periods; (c–e) Confocal microscopic images of NO release in A549 and LLC cells (c) treated with different samples for 48 h and semi-quantitative data of A549 (d) and LLC (e) cells after post-treatment. Dosage: 0.5 mg/mL, and scale bar: 50 μm; (f,g) Total nitric oxide content in A549 (f) and LLC (g) cells treated with different samples for 48 h. Dose: 0.5 mg/mL; (h–l) Proliferation (h,i), colony formation (j) and early apoptosis (k,l) of LLC cells treated with different samples alone (h,j,k) or combining with nitric oxide scavenger (NO–S) (i,j,l); (m,n) FCM patterns (m) and quantitative analysis (n) for determining DC maturation stained with CD80 and CD86 after different sample treatments for 12 h (dose: 0.5 mg/mL); (o–q) Secretion levels of TNF-α (o), IL-6 (p) and IL-12p70 (q) by DCs after various sample treatments for 12 h (dose: 0.5 mg/mL), and these data were detected by ELISA using LPS treatment as a positive control; (r) Apparatus schematic illustration of the transwell co-culture system: A549 cells and their residues were placed in the upper compartment and DCs were cultured in the lower compartment; (s–u) Secretion levels of TNF-α (s), IL-12p70 (t) and IL-6 (u) in DC suspensions after different treatments by ELISA. The data are presented as the mean ± SD (n = 3). 'NS' means no significance, $^{*}P < 0.05$, $^{**}P < 0.01$, $^{***}P < 0.001$ and $^{****}P < 0.0001$.

the sequential immunotherapy enabled by Mon@LA-PDE5i@M ATVs alone or Mon@LA-PDE5i@M plus anti-PD-L1. Moreover, *in vivo* nitric oxide expression of treated tumor tissues after immunofluorescence staining was tracked. Identical to *in vitro* results, the pluripotent ATVs significantly increase NO expression especially after uniting with PD-L1 blockade (Fig. 6g).

2.6. Sequential immunotherapy enabled by pluripotent ATVs alone or plus anti-PD-L1 for suppressing tumor metastasis on subcutaneous model

Tumor metastasis is the major obstacle leading to treatment failure, which seriously affects the prognosis of lung cancer patients. Therefore, we also took full advantage of the sequential immunotherapy-activated immune responses arising from PDE5&PD-L1 co-inhibition-mediated immunosuppressive microenvironment alleviation and the pluripotent ATVs-enhanced activation and infiltration of CTLs to inhibit metastasis on a bilateral LLC tumor-bearing mice model (Fig. 6h). Based on PDE5i-activated systematic immune responses, LA-originated NO toxicity and the enhanced PDE5i efficacy, PDE5i-involved ATVs alone can suppress the tumor growth and metastasis to some extent. Intriguingly, Mon@LA-PDE5i@M ATVs plus anti-PD-L1 doses the best job in almost completely eradicating the primary LLC tumor and significantly suppressing the metastasized ones (Fig. 6i–p), which suggests that the sequential immunotherapy enabled by the pluripotent ATVs-activated abundant CTLs infiltration and PDE5&PD-L1 co-inhibition probably brings about immune escape blockade and generates the robust immune memory effect. In addition, no abnormal weight change is found after ATVs treatment (Fig. S4). Results indicate that the infiltration of $CD3^+$ $CD8^+$ T cell in the distant tumors is indeed significantly upregulated in Mon@LA-PDE5i@M plus anti-PD-L1 group (Figure 6q). The variation trend of tumor volume was consistent with that of tumor weight, wherein Mon@LA-PDE5i@M combined with anti-PD-L1 blockade acquires the largest decreases of tumor weight and volume in both primary and distant tumors.

2.7. Sequential immunotherapy enabled by pluripotent ATVs plus anti-PD-L1 for suppressing orthotopic lung tumors and lung metastasis

Furthermore, orthotopic LLC tumor models mimicking human lung cancer were employed to assess the anti-metastasis efficiency of pluripotent ATVs-unlocked sequential immunotherapy. The biodistribution of Mon@LA-PDE5i@M ATVs was firstly evaluated, and high accumulation in lung is observed (Fig. 2i). In terms of anti-tumor evaluation, the inhibitory outcome against the orthotopic tumor model is approximately identical to that in the subcutaneously xenograft tumor model. Benefiting from the contributions of ATVs-activated abundant CTLs infiltration and PDE5&PD-L1 co-inhibition, the constituted sequential immunotherapy was equipped with the most robust anti-tumor ability.

IVFIS was introduced to track the migration pathway of *i.v.* injected RFP-LLC tumor cells. The bioluminescence imaging reveals that mice treated with pluripotent ATVs combing with anti-PD-L1 exhibit negligible bioluminescence signals, indicating the substantially suppressed tumor growth (Fig. 7a). To directly evaluate tumor variation, lungs in all groups were collected. The gross appearance of lung nodules reveals that Mon-PDE5i, Mon@LA-PDE5i@M and Mon@LA-PDE5i@M plus PD-L1 blockade prevent lung metastasis (Fig. S5a) and H&E staining-derived pathological analysis of the sectioned tissues also validates it (Fig. S5b). Quantitative results confirm that the sequential immunotherapy consisting of ATVs-unlocked CTLs activation and filtration and PDE5&PD-L1 co-inhibition-alleviated immunosuppressive microenvironment substantially reduces lung weight (Fig. S5c). Moreover, the proportions of $CD4^+$ and $CD8^+$ T cells in PBMCs are upregulated in ATVs alone and ATVs plus anti-PD-L1 groups (Fig. 7b–d). The proportion of antigen-specific $IFN\gamma^+$ that can stimulate $CD8^+$ T cells is significantly increased in tumor-bearing mice treated with Mon@LA-PDE5i@M ATVs plus anti-PD-L1 group. As well, $IFN\gamma^+CD4^+$T cells are significantly increased, suggesting that Mon@LA-PDE5i@M ATVs induces *in-situ* tumor immune responses to effectively generate tumor-specific T cell responses (Fig. 7e–h). Moreover, Mon@LA-PDE5i@M ATVs significantly increase infiltrated cytotoxic $CD8^+$ T cells and reduce $CD4^+$ T cells in tumor tissues (Figs. S5d–f). Moreover, antibody-mediated $CD8^+$ T cell exhaustion liberates immune escape and makes such pluripotent ATVs inhibit re-growth (Fig. 7i–k), which further confirms the role of $CD8^+$ T cells in tumor control.

In anti-PD1/PD-L1 immunotherapy, two concerns are highlighted, *i.e.*, other immunosuppressive targets-mediated immune escape and insufficient CTLs infiltration into tumor stroma [15–22]. PDE5 is a member of the phosphodiesterases (PDEs) that blocks second messenger signaling related to cyclic adenosine monophosphate and cyclic guanosine monophosphate (cGMP) [29,30]. In this study, we identified PDE5 as a poor prognostic predictor in lung adenocarcinoma patients, and it also serves as an immunosuppressive target in lung tumors. It is expected that blockading PDE5 can repress lung tumorigenesis. Adequate experimental results confirmed that PDE5i exhibited inhibitory efficiency against lung cancer in both *in vitro* and *in vivo* assays. PDE5 singling pathways are closely associated with NO and NO can serve as an immune enhancement agent for boosting immunotherapy [24,31–33]. Regarding this, LA as the endogenous NO donor is justifiably believed to be qualified for enhancing PDE5i-activated immune responses *via* generating abundant NO or cGMP [34].

To improve the bioavailability of LA and PDE5i *in vivo*, we encapsulated them in MON carrier [25], followed by TCM coating to obtain the pluripotent ATVs. LA introduction enabled the PDE5i/LA co-loaded ATVs to attain more excellent tumor growth inhibition both *in vitro* and *in vivo* compared to only PDE5i-loaded counterpart. More significantly, TCM-engineered ATVs allowed effective antigen presentation by APCs, activated DCs and CTLs, and promoted adequate CTLs infiltration to execute the killing effect towards PDE5&PD-L1 camouflage-free tumor cells. As well, TCM-mediated tumor tropism permitted more ATV internalizations by lung cancer *in vitro* and *in vivo*. Consequently, LA&PDE5i co-loaded ATVs promoted iNOS expression both in tumor cells and DCs and brought about robust cytotoxic effects and anti-tumor immune responses against lung tumor by producing abundant NO. Deeper investigation suggested that PDE5i could activate iNOS–NF–κB and cGAS signaling in DCs, agreeing with a previous study where PDE5i (*e.g.*,

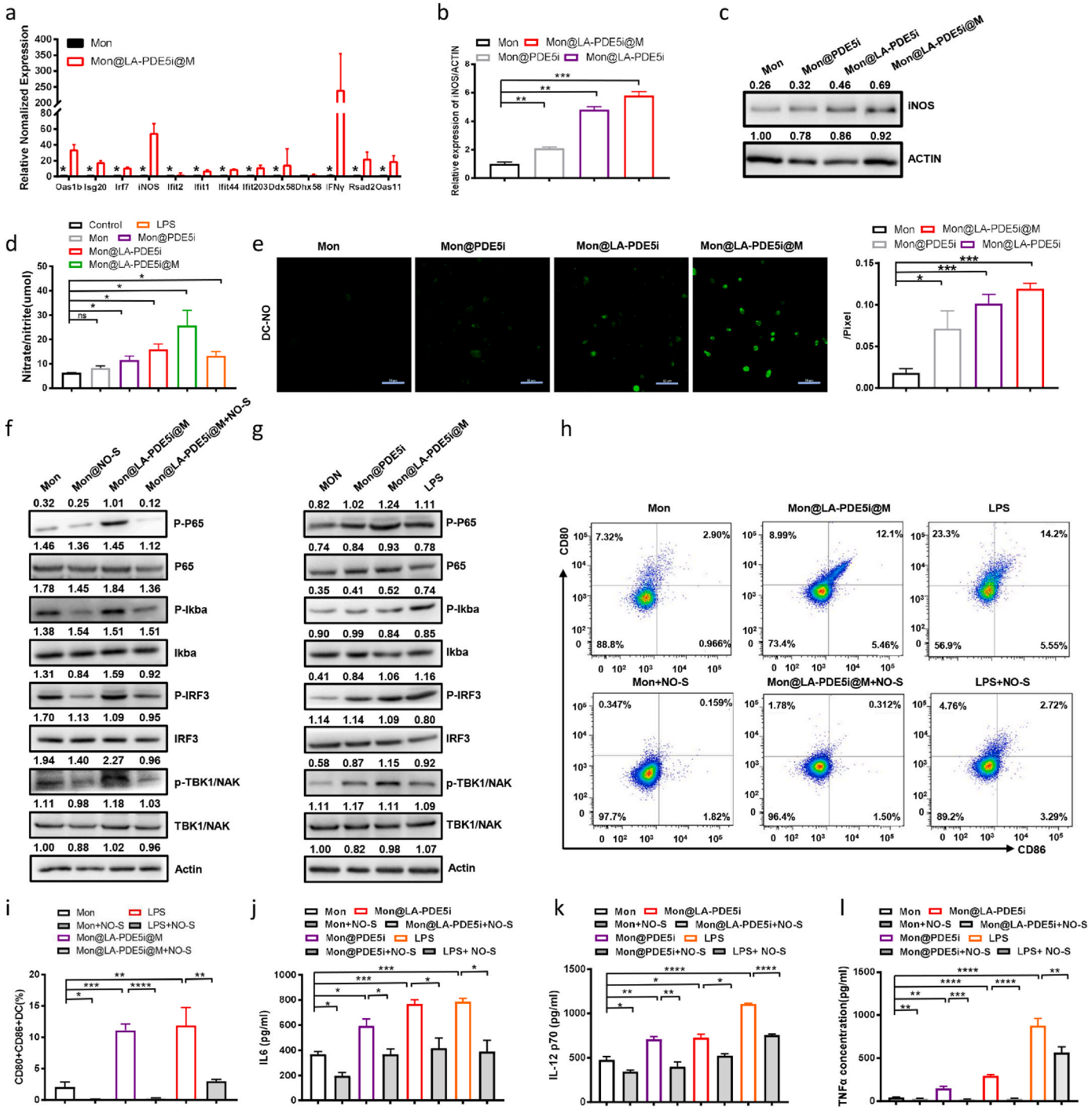

Fig. 5. In-depth and comprehensive explorations on such a pluripotent ATVs-enabled sequential immunotherapy for enhancing systematic anti-tumor immune responses *via* inspecting related genes and singling pathways. (a) qRT-PCR data that shows the expressions of a cluster of genes relating to DC maturation after Mon@LA-PDE5i@M treatment; (b) qRT-PCR data that shows the gene expression of iNOS in DCs after various treatments for 12 h (dose: 0.5 mg/mL); (c) Immunoblotting analysis of iNOS expression in DCs after various treatments; (d) Nitric oxide content in DCs after various treatments; (e) LCSM images of DCs after various treatments for evaluation NO production, and scale bar:50 μm; (f) Immunoblotting analysis of indicated proteins in DCs treated with different samples for 12 h, where actin was used as the loading control; (g) Immunoblotting analysis of indicated proteins in DCs treated with different nanoparticles with or without NO–S for 12 h; (h,i) Representative FCM patterns (h) and quantitative data analysis (i) for assessing matured DCs ($CD80^+CD86^+$) after different treatments for 12 h; (j–l) ELISA analysis of secretion levels of IL-6 (j), IL-12p70 (k) and TNF-α (l) in DCs suspensions after treatment with different samples combining NO–S or not. The data are presented as the mean ± SD (n = 3). 'NS' means no significance, $^*P < 0.05$, $^{**}P < 0.01$, $^{***}P < 0.001$ and $^{****}P < 0.0001$.

sildenafil) enhanced eNOS expression in endothelial cells [35]. In addition, the critical role of NO in modulating the cytotoxic effects was verified directly, and its immune activation degree was reflected by adding NO–S. In terms of the immune activation, PDE5i for improving innate or adaptive immune responses was further studied *via* examining the infiltrated lymphocytes subtypes in tumor tissues, DC maturation ($CD80^+CD86^+$) and T cell subtypes in the blood. Our results sufficiently demonstrated that the pluripotent ATVs could repress tumor growth *via* boosting the adaptive immune activation, *e.g.*, (i) altering myeloid phenotype including IL6, IL12 and TNFα production that could drive DC

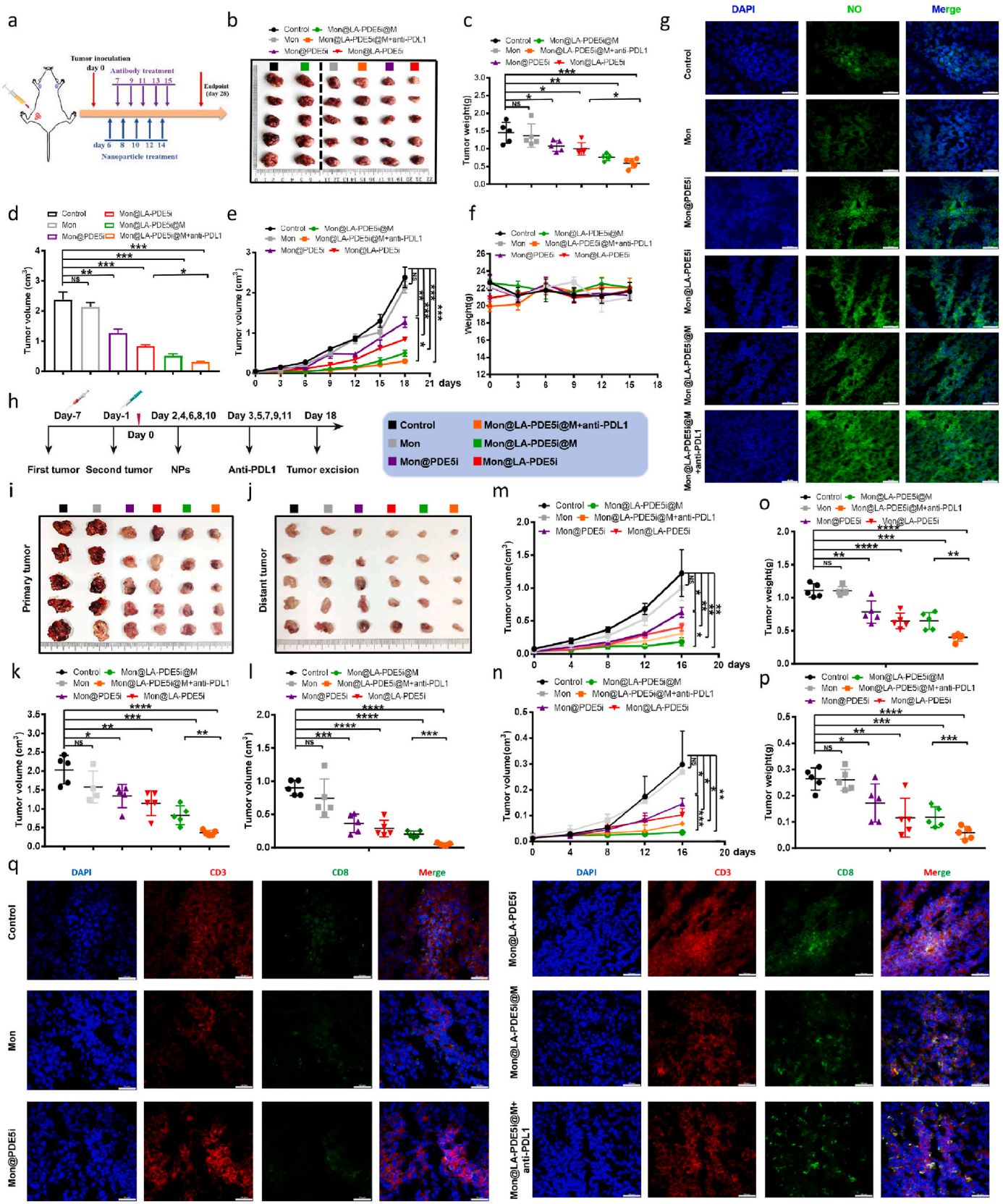

(caption on next page)

Fig. 6. *In vivo* sequential immunotherapy potentiated by pluripotent ATVs plus anti-PD-L1 for suppressing LLC primary and distant subcutaneous LLC tumors *via* PDE5&PD-L1 co-inhibition-arised immunosuppressive microenvironment alleviation and TCM-enhanced activation and infiltration of CTLs. (a) Schematic illustration of the experiment design for assessing the anti-tumor ability of Mon@LA-PDE5i@M ATVs plus anti-PD-L1 on unilaterally-inoculated LLC tumor models; (b–f) Anti-tumor outcomes against the LLC xenografted tumors in male C57/BL6 mice treated with different samples including tumor photos (b), average tumor weight (c), tumor volume (d) at the end of experimental period and the time-dependent variation curves of tumor volume (e) and body weight (f); (g) Representative LCSM images of NO in tumor slices after staining with NO indicator post-different sample treatments, and scale bar: 50 μm; (h) Schematic illustration on the anti-tumor experiment procedures against primary tumor and distant tumor on the bilaterally-inoculated tumor metastasis models; (i,j) Digital photographs of excised primary (i) and distant (j) tumors harvested from LLC xenografted bearing C57/BL6 mice treated with different samples at the end of experimental period; (k–p) Anti-tumor outcome evaluations against primary and distant LLC tumors subcutaneously transplanted in mice after different treatments, which including average volumes of primary (k) and distant (l) tumors at the end of experimental period, average weights of primary (m) and distant (n) tumors at the end of experimental period and time-dependent volume variation profiles of primary (o) and distant (p) tumors; (q) Representative LCSM images of $CD3^+CD8^+$ T cells in the distant tumor slices after immunofluorescence staining post-different treatments, and scale bar: 50 μm. The data are presented as the mean ± SD (n = 5). 'NS' means no significance, $^*P < 0.05$, $^{**}P < 0.01$, $^{***}P < 0.001$ and $^{****}P < 0.0001$.

maturation, and (ii) upregulating $CD8^+$ T cell population in blood and tumor tissues that could result in high IFNγ expression.

Taken all together, the pluripotent ATVs-unlocked sequential immunotherapy was constituted of PDE5 immunosuppressive microenvironment alleviation especially in the presence of LA-enhanced PDE5i efficiency and TCM-enhanced CTLs infiltration. Significantly, anti-PD-L1 introduction further potentiated the sequential immunotherapy, which provided distinctive insights into the immune response elevation and immune escape blockade. ATVs-enabled PDE5 inhibition along with PD-L1 blockade synergistically eradicated local and abscopal lung cancers in orthotopic and subcutaneous models, performing much better than either PD-L1 blockade alone or PDE5 inhibition alone. This dual-target co-inhibition strategy maximally magnified the immune responses. These results adequately suggest that the unprecedented advances of nanobiotechnology will guide and boost the performance of many treatment methods against tumor or other lesions after absorbing abundant experiences [36–40].

3. Conclusions

In summary, we screened out PDE5 as a new immunosuppressive target in lung tumors, and constructed TCM-coated pluripotent ATVs that co-encapsulated PDE5i and LA to blockade PDE5 and enhanced the activation and infiltration of CTLs, establishing the ATVs-unlocked sequential immunotherapy approach. Uniting with massive ATVs accumulation arised from TCM-mediated tumor tropism, this ATVs-unlocked sequential immunotherapy exerted the potent anti-tumor activity *via* enhancing immune responses including DC maturation and $IFN\gamma^+CD8^+$ T cell population. In particular, the co-loaded LA potentiated the PDE5i-activated anti-tumor immune responses *via* elevating NO release, iNOS and cGMP expressions, consequently contributing to the considerably-intensified anti-tumor consequences. Impressively, the pluripotent ATVs plus anti-PD-L1 maximally magnified immune responses and inhibited immune escape, which not only eradicated the primary tumor, but also caused systemic anti-tumor immunity to efficiently repress distantly metastasizing ones in both orthotopic and subcutaneous lung tumor models. These appealing results underscore the clinical translation potential and availability of pluripotent ATVs or plus anti-PD-L1. Such a ATVs-enabled sequential immunotherapy constituted of PDE5&PD-L1 co-inhibition-arised immunosuppressive microenvironment alleviation and TCM-enhanced activation and infiltration of CTLs can also serve as a general anti-tumor method for addressing the suffering (*i.e.*, low treatment efficiency) that single PD-1/PD-L1 immunotherapy encountered.

4. Materials and methods

4.1. Patients and tissue samples

A total of 8 matched lung cancer tissues and adjacent normal tissues were collected from patients who were treated in the Sichuan cancer hospital between 2015 and 2018. The patients' basic information was provided in Table S1. Both lung adenocarcinoma and paired normal tissues (taken at least 5 cm from the tumor were confirmed to be normal by histological examination) were analyzed for PDE5 protein expression by Western blot. Human lung adenocarcinoma tissue array was purchased from Shanghai Biochip Company Ltd (Shanghai, China), of which 81 cases with survival information were used for immunohistochemistry and survival analysis and the lung adenocarcinoma patients' survival information was concluded in Table S2. The use of all patient specimens was approved by the ethics committee of Sichuan cancer hospital.

4.2. Cell line and animals

Human LAC cell lines A549, H1975, H1299, H358, mice lung cancer cell line LLC and human pulmonary epithelial cell (HBE) were purchased from the ATCC and cultured in Dulbecco's modified Eagle's medium (DMEM) supplemented with 10% fetal bovine serum (FBS) and 100 U/mL penicillin–streptomycin. The cells were maintained in a humidified 37 °C incubator with a 5% CO_2 atmosphere. Male C57/BL6 mice (6–8 weeks) were maintained under protocols approved by Institutional Animal Care and Use Committee of the Sichuan Cancer Hospital. BMDCs collected from marrow G cavities of femurs and tibias of 8–10 weeks-old C57/BL6 mice were cultured in culture dishes containing 4 mL serum-containing RPMI 1640 medium with 100 mg/mL streptomycin, 100 IU/mL penicillin, 10 ng/mL GM-CSF, 10 ng/mL IL-4 for 8 days.

4.3. Characterization of different sample formulations

The hydrodynamic diameters of NPs suspended in 1 × PBS were measured by dynamic light scattering (DLS) (Malvern Instruments, UK). The morphology of Mon@LA-PDE5i@M was characterized by transmission electron microscope (TEM, JEM-1230, Japan). TEM imaging of those membrane-coated NPs was carried out directly without using any staining. The protein contents in membrane-coated Mon@LA-PDE5i were determined by the western blot assay.

4.4. Quantitative real-time PCR (qRT-PCR) test

Total RNA extracted from cancer cells using Trizol Reagent (Invitrogen, USA), and qRT-PCR was performed using SYBR Prime Script RT-PCR kit (TaKaRa, Japan) on a Rotor-Gene 6000 real-time genetic analyzer (Corbett Life Science, USA). The primer sequences and the product sizes listed in Table S3 β-Actin was used as the internal control. The PCR conditions were set as follows: denaturation at 95 °C for 2 min, followed by amplification for 40 cycles and quantification (95 °C for 5 s, 55 °C-57 °C for 30 s), and melting curve (55 °C-95 °C with 0.5 °C increment each cycle). Each sample was tested in triplicates.

4.5. Immunoblotting analysis

Immune blot analysis used to identify indicated protein expression in cell lines and tissues. Immune blot performed as previously described.

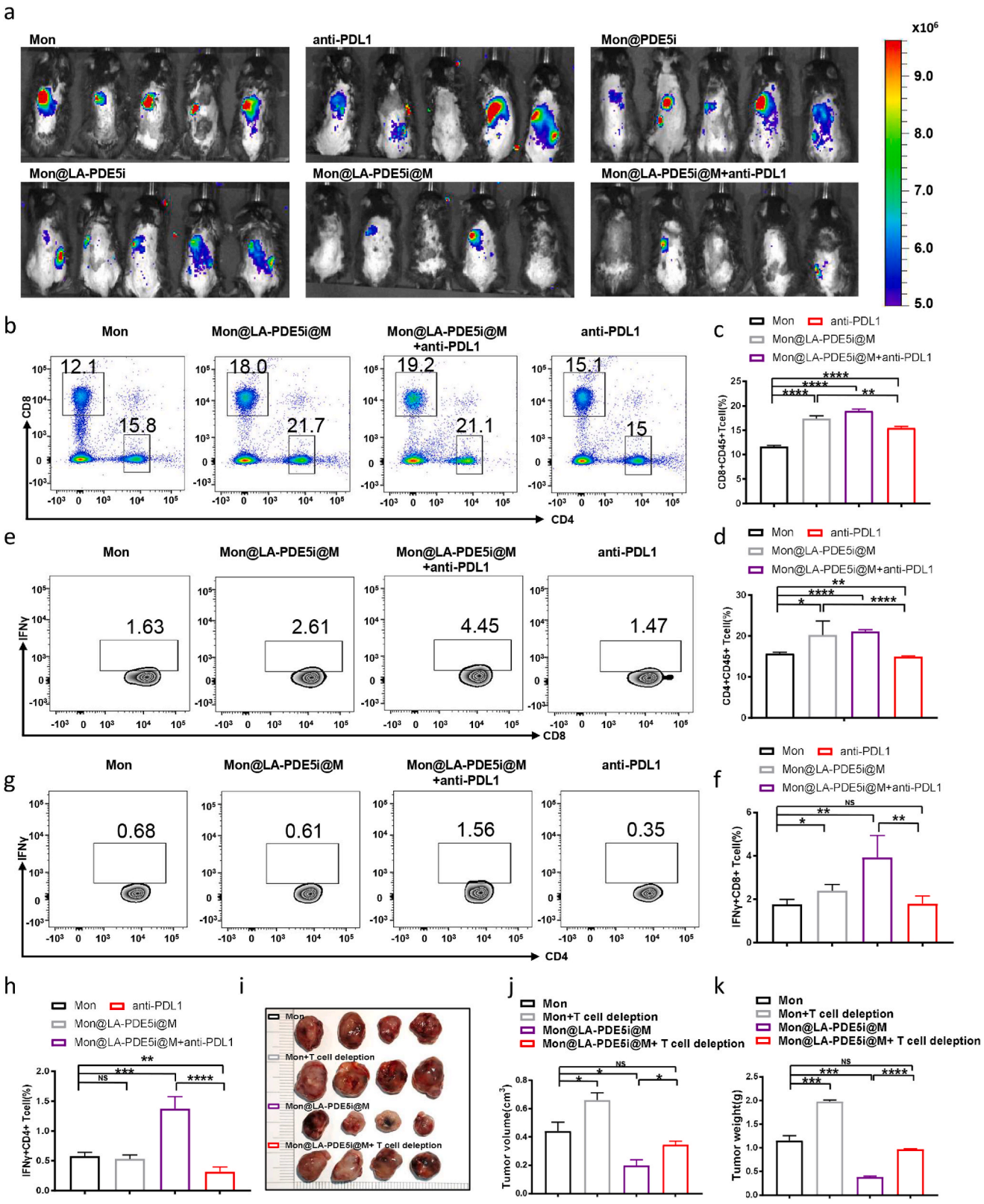

Fig. 7. Sequential immunotherapy potentiated by pluripotent ATVs plus anti-PD-L1 for suppressing orthotopic tumors and tumor metastasis *via* PDE5&PD-L1 co-inhibition-arised immunosuppressive microenvironment alleviation and TCM-enhanced activation and infiltration of CTLs. (a) *In vivo* bioluminescence images of male C57/BL6 mice for tracking the migration and growth of *i.v.* injected RFP-LLC tumor cells after different treatments; (b–h) Representative FCM plots for quantifying the subtypes in PBMCs (b), which include $CD8^+$ T cells ($CD45^+CD8^+$) (c), $CD4^+$ T cells ($CD45^+CD4^+$) (d), $CD45^+CD8^+IFN\gamma^+$ (e,f) and $CD45^+CD4^+IFN\gamma^+$ (g,h) in the tumor-bearing mice treated with Mon or Mon@LA-PDE5i@M alone or plus anti-PD-L1. The data are presented as the mean ± SD (n = 5); (i–k) Digital photos (i), average volume (j) and average weight (k) of excised subcutaneously transplanted LLC tumors harvested from tumor-bearing mice after various treatments uniting with or without $CD8^+$ T cells exhaustion at the end of experimental period. The data are presented as the mean ± SD (n = 4). 'NS' means no significance, $^*P < 0.05$, $^{**}P < 0.01$, $^{***}P < 0.001$ and $^{****}P < 0.0001$.

The prepared A549 membrane and whole A549 cells were scraped from the culture, and lysed (RIPA: PMSF = 100:1) in an ice bath for 30 min. Centrifuge at 15000 g for 15 min, collect the supernatant and add 5 × loading buffer, and heat at 100 °C for 10min. The primary antibodies were as follows: NA^+/K^+-ATPase (1 : 1000, CST, Catalog: #3010, USA); LaminB1 (1 : 1000, CST, Catalog: #13435, USA); Ki-67 (1 : 1000, CST, Catalog:#13435, USA); β-actin (1 : 1000, CST, Catalog: #4970, USA); E-cadherin (1 : 1000, Abclonal, Catalog: #A11 492, China); GAPDH (1 : 1000, CST, Catalog: #5174, USA); COX-IV (1 : 1000, CST, Catalog: #4850, USA); NF-κB p65 (1 : 1000, CST, Catalog: #8242, USA); P-p65(1 : 1000, CST, Catalog: #3033, USA); IkBa (1 : 1000; CST, Catalog: #9242, USA); p-IkBa (1 : 1000, CST, Catalog: #2859, USA); IRF3 (1:1000, CST, Catalog: #4302, USA); P-IRF3 (1:1000, CST, Catalog: #29047, USA); TBK1/NAK (1 : 1000, CST, Catalog: #38066, USA); P-TBK1/NAK (1 : 1000, CST, Catalog: #5483, USA); anti-β-actin (1 : 1000, CST, Catalog: #38066,USA); PDE5 (1 : 1000, Abcam, Catalog: #ab64179, USA); iNOS (1 : 1000, Abcam, Catalog: #ab178945, USA). Antibody was detected using a horseradish peroxidase (HRP)-conjugated goat anti-mouse IgG kappa secondary antibody (1: 1000, CST, Catalog: #7076, USA) or horseradish peroxidase (HRP)-conjugated goat anti-Rabbit IgG kappa secondary antibody (1: 1000, CST, Catalog: #7074, USA).

4.6. Cell proliferation assay

Cancer cells were seeded in 96-well plates at 2×10^3 cells per well in 0.2 mL of DMEM medium containing 10% FBS. Different samples were added in the culture media with a fixed concentration of 0.5 mg/mL for 48 h at 37 °C and 5% CO_2, followed by the designated treatments, then replaced by the DMEM medium containing 10% FBS for 5 days. In the following 5 days, the MTT assay performed daily. MTT [3-(4,5-dimethylthiazol-2-yl)-2,5-diphenyltetrazoli um bromide] solution (50 μL, 2 mg/mL, Sigma-Aldrich, USA) was added to cell culture, followed by incubation at 37 °C for 2 h. Culture medium was replaced by 150 μL DMEM and optical density was measured based on the absorbance at the wavelength of 450 nm by using a microplate reader (Bio-TekELx800, USA).

4.7. Apoptosis assay

For apoptosis assays, cells were treated with different samples for 48 h (dose: 0.5 mg/mL), following by nitric oxide scavenger treatment or not, then collected and washed twice with cold PBS, and re-suspended in binding buffer at a concentration of 1×10^6 cells/mL. 500 μL of cell suspension was transferred to a 2 mL culture tube. 5 μL of Annexin V-FITC were added to each tube. Cells were incubated at room temperature (25 °C) for 15 min in a dark environment, and then analyzed on FACS Calibur (BD Biosciences, USA), and results were calculated using Cell Quest software (BD Biosciences, USA).

4.8. Nitric oxide scavenging

For nitric oxide scavenging, the hemoglobin (S0017, Beyotime, China) was added in the culture media at a concentration of 20 μM/mL for 12 h, followed by different treatments in the proliferation, colony formation, apoptosis and DC cells maturation assay.

4.9. Enzyme-linked immunosorbent assay (ELISA)

The levels of IL-6, IL-12p70 and TNF-α in serum and conditioned media were detected using ELISA kit in accordance with the manufacturer's instructions (IL-6: M6000B; IL-10: M1000B; TGF-β1: MB100B; R&D Systems Co., Ltd., USA). The ELISA plate was treated and incubated with 50 μL of bovine serum albumin (BSA) blocking solution (10 mg/mL), 50 μL of serum and 50 μL of biotin-conjugated detector mAb were mixed at 37 °C for 1 h, and mixed with avidin-HRP solution (1:100). After final rinsing with PBST, 100 μL of tetramethylbenzidine (TMB) substrate solution (10 mg/mL) was added for color reaction with Ag-Ab complex. The relative absorbance at 450 nm was measured using an automated ELISA reader (Bio-Rad model 550, Irvine, CA). The concentration was determined by comparing optical density value with standard curve.

4.10. HE staining

For morphometric analysis, transverse sections (5 μm in thickness) were stained with hematoxylin and eosin (HE) staining. The slices were deparaffinized in xylene, which were treated in gradient concentrations of ethanol, rinsed for 1 min, stained with hematoxylin staining solution (Harris) for 3 min, and then differentiated with 0.8% hydrochloric acid. Ultimately, they were stained with eosin stain (alcohol-soluble) for 20 s, directly treated with absolute ethanol for 1 min, transparentized and sealed.

4.11. Immunofluorescence staining

Cells were blocked with pre-immune goat serum at 37 °C for 30mins, and then incubated with primary antibodies at 4 °C overnight. Antibody information used in the experiments will be provided upon request. The cells were subsequently washed in PBS and incubated at 37 °C for 1h with Cy3 or Cy5-conjugated goat anti-rabbit or anti-mouse IgG antibodies (1:1000; Invitrogen, USA). Nuclei were counterstained with Hochest 33258. Cells were observed under laser confocal scanning microscopy (LCSM, Leica TCS-SP5, Germany). Additionally, frozen sections were incubated with monoclonal anti-CD3 antibody (1:200, Abcam, Catalog:#ab16669, USA) and monoclonal rabbit anti-CD8 antibody (1:200, Abcam, Catalog:#ab217344, USA) for over-night (4 °C), followed by incubation with secondary antibody. The immunofluorescence images were imported into Image-Pro Plus 6.0 software for further analysis.

4.12. Immunohistochemistry (IHC) analysis

Immunohistochemical staining was performed on tissue array slides and tumor xenografts using the streptavidin–biotin–peroxidase complex method. The antigen retrieval procedure was performed by heating the samples in antigen retrieval solution containing 10 mM sodium citrate buffer with a pressure cooker. Rabbit anti-human PDE5 antibody (abcam, ab64179, 1:100) was used to detect PDE5. Slides were counterstained with hematoxylin (Sigma). IHC staining intensity was independently scored by two anatomical pathologists. The staining intensity (negative = 0, weak = 1, moderate = 2, or strong = 3 scores) and the proportion of positive cells rounded of interest (<25% = 1, 25–50% = 2, >50% to <75% = 3, ≥75% = 4) were scored. The immunostaining was semi-quantitatively categorized by combining the intensity and the quantity scores, which yielded a staining index (values from 0 to 12). The staining index of 8–12 was regarded as high expression, while the staining index below 6 was considered as low expression.

4.13. Preparation of Mon@LA-PDE5i@M ATVs

According the manufacture (Thermo-fisher, USA), the A549 or LLC membranes were prepared by a membrane protein extraction kit. The resulting packed A549/LLC membrane was washed once in cold 1 × PBS. Afterwards, A549/LLC membrane was re-suspended in 1 × PBS and mixed with Mon@LA-PDE5i at 4 °C overnight. To obtain mannose-inserted A549/LLC membrane, the solution was stirred with DSPE-PEG-Man (0.1 mg/mL) for 1 h, where DSPE-PEG-Man was thus inserted into A549/LLC cell membranes according to a previous protocol. Then, the mixture was saved in 1 × PBS solution.

4.14. Nitric oxide fluorescence quantitative detection

Detection of total nitric oxide content in A549 (g) and LLC (h) cells were treated with ATVs for 48 h. The intracellular nitric oxide production level was detected by 3-Amino, 4-aminomethyl-2′,7′-difluorescein, diacetate (DAF-FM DA) according to the manufacture (Beyotime, Catalog:#S00019, Shanghai, China). Different samples (*i.e.*, Mon, Mon@-PDE5i, Mon@LA-PDE5i, Mon@LA-PDE5i@M) were set to explore their potential in producing nitric oxide. In brief, cell culture medium was removed from A549, LLC or DC cells and diluted DAF-FM DA (5 μmol/L) was added. The added dose was adjusted to completely cover the cells, and the volume of diluted DAF-FM DA that was added to each hole in the six-hole plate was usually 1 mL. The cells were incubated in a cell incubator at 37 °C for 20 min. Subsequently, cells were washed with PBS (pH = 7.4) three times to fully remove residual DAF-FM DA that did not enter the cells, and then observed by LCSM. Furthermore, the Total Nitric Oxide Assay Kit (Beyotime, Catalog: #S00024, Shanghai, China) was used for quantitatively detecting intracellular nitric oxide level according to the manufacture reference.

4.15. In vitro DC activation and cytokine analysis

DCs (1×10^6 cells) were incubated with NPs for 24 h. FCM analysis was performed to analyze the percentages of matured DCs. Cells suspended in PBS containing 1% FBS were incubated with anti-mouse antibody against CD80-APC (ebioscience, Catalog: #2036646, USA), and CD86-PE-cy7 (ebioscience, Catalog: #2050424, USA) for 30 min at 4 °C in the darkness and then evaluated by FCM. For quantitative release of IL-6, TNF-α and IL-12p40, the DC supernatants were measured by ELISA following the vendor's protocol (Beyotime Biotechnology).

4.16. In vitro DC stimulation transwell co-culture experiment

The Millicell Cell Culture Insert (0.4 μm, sigma, USA) was used for the co-culture assay to investigate DC maturation *in vitro*. A549 cancer cells (5×10^4) treated with different samples at a concentration of 0.5 mg/mL were placed in the upper for 48 h, and then bone marrow derived dendritic cells (DCs) were placed in the lower chamber. Lipopolysaccharide (LPS, Sigma) at a dose of 1 μg/mL was used as the positive control. DCs stained with anti-CD86 PE-cy7 (ebioscience, Catalog: #2050424, USA) and anti-CD80 APC (ebioscience, Catalog: #2036646, USA) were analyzed by FCM. The pro-inflammatory cytokines (*i.e.*, IL-6, IL-12p70 and TNF-α) from DC suspensions were tested by using ELISA kits with a standard protocol.

4.17. In vivo therapeutic effect of ATVs plus anti-PDL1 blockade on subcutaneously xenografted tumor model

Four-week-old male C57/BL6 mice were approved by the Institutional Animal Care and Use Committee of the Sichuan Cancer Hospital. The number of 1×10^6 LLC cells was suspended in 50 μL of PBS and subcutaneously implanted in male mice. All the tumor-bearing mice were randomly divided into several groups for different treatments: PBS, Mon, Mon@LA, Mon@PDE5i, Mon@LA-PDE5i, Mon@LA-PDE5i@M, Mon@LA-PDE5i@M+anti-PD-L1, anti-PD-L1. Mice in each group were injected with different samples sharing identical PDE5i dose (100 mg/kg mice) *via* tail vein once per two days for five repeated injections in total. For anti-PDL1 injection, mice were intravenously administrated with anti-PD-L1 (75 μg per mouse for each injection) after 24 h post-PDE5i-involved injections. The size of the xenografted tumor was measured every 3 days using a Vernier calliper, and the volume was calculated at different indicated intervals post-transplantation as follows: volume = shortest diameter^2 × longest diameter/2. At the end of experimental periods, the subcutaneous xenografted tumors were collected and weighed. The anti-metastasis evaluation was implemented on another subcutaneously xenografted tumor.

4.18. In vivo anti-metastasis exploration of ATVs plus anti-PDL1 blockade on subcutaneously distant and orthotopic tumor models

The first tumor inoculation, LLC cells (1×10^6) were subcutaneously injected into the right flank of each C57/BL6 mouse. Six days later, the tumor-bearing mice were randomly divided into six groups (n = 5), and LLC cells were subcutaneously injected into the left inguina of each mouse for the second tumor inoculation and served as the artificial model of metastasis. Different samples were *i.v.* injected into animals at the same doses as mentioned above (once per two days for 5 times in total, dose: 100 mg PDE5i/kg mice), and anti-PDL1 antibodies at the dose of 75μg/mouse were intraperitoneally administered on the next day. At the end of the experiment period, mice were killed and tumors were excised, weighed and photographed. To establish the lung metastasis model, RFP-LL Cells (1×10^5) were administered intravenously *via* tail vein infusion. Then ATVs and anti-PD-L1 treatment were administrated as above mentioned. An *in vivo* imaging spectrum system was used for the bioluminescence imaging after 60000 ms exposure. Lung micrometastases in five lobes were counted directly through microscopic observation, and afterwards they were studied by pathological analysis.

4.19. Fluorescence visualization

For intravital imaging and assessment of bio-distribution, cyclodextrin-labeled ATVs were used. The bio-distribution of Mon@LA-PDE5i@M in C57BL/6 mice was immediately determined by time-lapse confocal fluorescence microscopy after tail vein injection of different samples (100 mg/kg, 50 μL saline). Time-lapse images were acquired continually within the initial 3 h after Mon@LA-PDE5i@M ATVs injection, after which the mice were allowed to recover before subsequent imaging at 6h. Surgically resected tissues of interest were thoroughly washed in PBS and placed in an OV100 (Olympus) for bright-field imaging to identify regions of interest and fluorescence reflectance imaging. Integrated fluorescence density of regions of interest (ROIs) was determined (ImageJ, NIH). Values were obtained after subtracting tissue autofluorescence (background) in a vehicle-treated control.

4.20. $CD8^+$ T cell exhaustion test

In $CD8^+$ T cell exhaustion experiments, mice received intraperitoneal injection of anti-mouse CD8a antibody (200 μg, clone 53–6.7, BE0004-1) or isotype control (200 μg, clone 2A3, BE0089). All antibodies used in *in vivo* experiments were obtained from BioXCell.

4.21. Flow cytometry (FCM) analysis

After the *in vivo* tumor treatment five times, tumor-draining lymph nodes were excised for FCM analysis after co-staining with anti-CD86 PE-Cy7 (ebioscience, Catalog: #2050424, USA) and anti-CD80 APC (ebioscience, Catalog: #2036646, USA). The tumor tissues were cleaved by type I and IV collagenase at 37 °C for 40 min and then filtered by a 0.45 μm filter and then suspended in PBS. The blood samples were collected and PBMCs were sorted by Ficoll. The harvested cells from tumor tissues and blood samples were further stained with fluorochrome-conjugated antibodies in the darkness under 4 °C for 30 min: Ms anti-CD45-APC Cy7(BD, Catalog: 557659), Ms anti-CD4-Percp–Cy5.5(BD, Catalog: 55095 4), Ms anti-CD8-APC (BD, Catalog: 553035), Ms anti-IFNγ-Alexa fluor@488 (BD, Catalog: 557724, Ms anti-CD86 PE-Cy7 (ebioscience, Catalog: #2050424, USA) and Ms anti-CD80 APC (ebioscience, Catalog: #2036646, USA) antibodies, and then analyzed by FCM.

4.22. Ethics approval and consent

Animal experiments were approved by the Institutional Animal Care and Use Committee of the Sichuan Cancer Hospital, China. Ethical

approval for data extraction and tissue microarray construction of patients with lung cancer was obtained from ethics committee of Shanghai Biochip Company Ltd.

4.23. Statistical analysis

Statistical analyses were performed using GraphPad Prism 6.0 (GraphPad, La Jolla, CA, USA). Two tailed unpaired *t*-test or one-way ANOVA were used to determine the level of significance. All data used in this study met the assumptions of statistical tests. Survival analyses were carried out using Kaplan–Meier curves with the log-rank test for comparison. All quantitative data were presented as Mean ± S.D. or mean ± S.E.M. as indicated. $P < 0.05$ was considered as statistical significance. All experiments were carried out at least in triplicate.

Author contributions

#H. Wu, H. Li and Y. Liu contributed equally to this work. K. Zhang, C. Xu and H. Wu conceived and designed the experiments. H. Wu, H. Li, Y. Liu and J. Liang performed the experiments. H. Wu, Q. Liu, J. Liang, and Y. Liu collected and analyzed the data. K. Zhang, C. Xu, Z. Chen, Z. Xu and X. Zhang provided suggestions and technical support on the project. C. Xu and K. Zhang supervised the project. K. Zhang, X. Zhang, H. Wu and C. Xu wrote and revised the manuscript. All authors discussed the results and commented on the manuscript.

Declaration of competing interest

The authors declare no competing financial interest.

Acknowledgements

This work was supported by the National Natural Science Foundation of China (82022033, 81873048, 81771836 and 82004006), Sichuan Provincial Science Fund for applied basic research of China (2020YJ0108) and Sichuan Provincial Science Fund for Distinguished Young Scholars of China (2020JDJQ0065).

Appendix A. Supplementary data

Supplementary data to this article can be found online at https://doi.org/10.1016/j.bioactmat.2021.10.048.

References

[1] S. Devalaraja, T.K.J. To, I.W. Folkert, R. Natesan, M.Z. Alam, M.H. Li, Y. Tada, K. Budagyan, M.T. Dang, L. Zhai, G.P. Lobel, G.E. Ciotti, T.S.K. Eisinger-Mathason, I.A. Asangani, K. Weber, M.C. Simon, M. Haldar, Tumor-derived retinoic acid regulates intratumoral monocyte differentiation to promote immune suppression, Cell 180 (2020) 1098–1114.

[2] D. Zhao, L. Cai, X. Lu, X. Liang, J.X. Li, P.W. Chen, M. Ittmann, X.Y. Shang, S. Jiang, H.Y. Li, C.L. Meng, I. Flores, J.H. Song, J.W. Horner, Z.D. Lan, C.J. Wu, J. Li, Q. Chang, K.C. Chen, G.C. Wang, P.N. Deng, D.J. Spring, Y.A. Wang, R.A. DePinho, Chromatin regulator CHD1 remodels the immunosuppressive tumor microenvironment in PTEN-deficient prostate cancer, Cancer Discov. 10 (2020) 1374–1387.

[3] E. Friebel, K. Kapolou, S. Unger, N.G. Nunez, S. Utz, E.J. Rushing, L. Regli, M. Weller, M. Greter, S. Tugues, M.C. Neidert, B. Becher, Single-cell mapping of human brain cancer reveals tumor-specific instruction of tissue-invading leukocytes, Cell 181 (2020) 1626–1642.

[4] H.L. MacGregor, A. Sayad, A. Elia, B. Wang, S.R. Katz, P.A. Shaw, B.A. Clarke, S. Q. Crome, C. Robert-Tissot, M.Q. Bernardini, L.T. Nguyen, P.S. Ohashi, High expression of B7-H3 on stromal cells defines tumor and stromal compartments in epithelial ovarian cancer and is associated with limited immune activation, J. Immunother. Cancer 7 (2019) 357.

[5] A.A. Barkal, R.E. Brewer, M. Markovic, M. Kowarsky, S.A. Barkal, B.W. Zaro, V. Krishnan, J. Hatakeyama, O. Dorigo, L.J. Barkal, I.L. Weissman, CD24 signalling through macrophage siglec-10 is a target for cancer immunotherapy, Nature 572 (2019) 392–396.

[6] R.L. Vartuli, H.B. Zhou, L.D. Zhang, R.K. Powers, J. Klarquist, P. Rudra, M. Y. Vincent, D. Ghosh, J.C. Costello, R.M. Kedl, J.E. Slansky, R. Zhao, H.L. Ford, Eya3 promotes breast tumor-associated immune suppression via threonine phosphatase-mediated PD-L1 upregulation, J. Clin. Invest. 128 (2018) 2535–2550.

[7] D.Y. Oh, S.S. Kwek, S.S. Raju, T. Li, E. McCarthy, E. Chow, D. Aran, A. Ilano, C.C. S. Pai, C. Rancan, K. Allaire, A. Burra, Y. Sun, M.H. Spitzer, S. Mangul, S. Porten, M. V. Meng, T.W. Friedlander, C.J. Ye, L. Fong, Intratumoral CD4(+) T cells mediate anti-tumor cytotoxicity in human bladder cancer, Cell 181 (2020) 1612–1625.

[8] W.W. Yue, L. Chen, L.D. Yu, B.G. Zhou, H.H. Yin, W.W. Ren, C. Liu, L.H. Guo, Y. F. Zhang, L.P. Sun, K. Zhang, H.X. Xu, Y. Chen, Checkpoint blockade and nanosonosensitizer-augmented noninvasive sonodynamic therapy combination reduces tumour growth and metastases in mice, Nat. Commun. 10 (2019) 2025.

[9] D.A. Braun, Y. Hou, Z. Bakouny, M. Ficial, M.S. Angelo, J. Forman, P. Ross-Macdonald, A.C. Berger, O.A. Jegede, L. Elagina, J. Steinharter, M. Sun, M. Wind-Rotolo, J.C. Pignon, A.D. Cherniack, L. Lichtenstein, D. Neuberg, P. Catalano, G. J. Freeman, A.H. Sharpe, D.F. McDermott, E.M. Van Allen, S. Signoretti, C.J. Wu, S. A. Shukla, T.K. Choueiri, Interplay of somatic alterations and immune infiltration modulates response to PD-1 blockade in advanced clear cell renal cell carcinoma, Nat. Med. 26 (2020) 909–918.

[10] D.Y. Torrejon, G. Abril-Rodriguez, A.S. Champhekar, J. Tsoi, K.M. Campbell, A. Kalbasi, G. Parisi, J.M. Zaretsky, A. Garcia-Diaz, C. Puig-Saus, G. Cheung-Lau, T. Wohlwender, P. Krystofinski, A. Vega-Crespo, C.M. Lee, P. Mascaro, C.S. Grasso, B. Berent-Maoz, B. Comin-Anduix, S. Hu-Lieskovan, A. Ribas, Overcoming genetically based resistance mechanisms to PD-1 blockade, Cancer Discov. 10 (2020) 1140–1157.

[11] H. Liu, X.W. Kuang, Y.C. Zhang, Y.Q. Ye, J.L. Li, L. Liang, Z.Z. Xie, L. Weng, J. Guo, H. Li, F.Y. Ma, X.D. Chen, S. Zhao, J. Su, N. Yang, F. Fang, Y. Xie, J. Tao, J. L. Zhang, M.L. Chen, C. Peng, L.Q. Sun, X. Zhang, J. Liu, L. Han, X.W. Xu, M. C. Hung, X. Chen, ADORA1 inhibition promotes tumor immune evasion by regulating the ATF3-PD-L1 Axis, Cancer Cell 37 (2020) 324–339.

[12] J.A. Moral, J. Leung, L.A. Rojas, J.N. Ruan, J.L. Zhao, Z. Sethna, A. Ramnarain, B. Gasmi, M. Gururajan, D. Redmond, G. Askan, U. Bhanot, E. Elyada, Y. Park, D. A. Tuveson, M. Gonen, S.D. Leach, J.D. Wolchok, R.P. DeMatteo, T. Merghoub, V. P. Balachandran, ILC2s amplify PD-1 blockade by activating tissue-specific cancer immunity, Nature 579 (2020) 130–135.

[13] J.C. Waite, B. Wang, L. Haber, A. Hermann, E. Ullman, X. Ye, D. Dudgeon, R. Slim, D.K. Ajithdoss, S.J. Godin, I. Ramos, Q. Wu, E. Oswald, P. Poon, J. Golubov, D. Grote, J. Stella, A. Pawashe, J. Finney, E. Herlihy, H. Ahmed, V. Kamat, A. Dorvilliers, E. Navarro, J. Xiao, J. Kim, S.N. Yang, J. Warsaw, C. Lett, L. Canova, T. Schulenburg, R. Foster, P. Krueger, E. Garnova, A. Rafique, R. Babb, G. Chen, N. S. Oristian, C.J. Siao, C. Daly, C. Gurer, J. Martin, L. Macdonald, D. MacDonald, W. Poueymirou, E. Smith, I. Lowy, G. Thurston, W. Olson, J.C. Lin, M.A. Sleeman, G.D. Yancopoulos, A.J. Murphy, D. Skokos, Tumor-targeted CD28 bispecific antibodies enhance the antitumor efficacy of PD-1 immunotherapy, Sci. Transl. Med. 12 (2020), eaba2325.

[14] T. Shukuya, V. Ghai, J.M. Amann, T. Okimoto, K. Shilo, T.K. Kim, K. Wang, D. P. Carbone, Circulating MicroRNAs and extracellular vesicle-containing MicroRNAs as response biomarkers of anti-programmed cell death protein 1 or programmed death-ligand 1 therapy in NSCLC, J. Thorac. Oncol. 15 (2020) 1773–1781.

[15] E.A. Ansa-Addo, H.C. Huang, B. Riesenberg, S. Iamaswat, D. Borucki, M.H. Nelson, J.H. Nam, D. Chung, C.M. Paulos, B. Liu, X.Z. Yu, C. Philpott, P.H. Howe, Z.H. Li, RNA binding protein PCBP1 is an intracellular immune checkpoint for shaping T cell responses in cancer immunity, Sci. Adv. 6 (2020) eaaz3865.

[16] D.G. Wang, T.T. Wang, H.J. Yu, B. Feng, L. Zhou, F.Y. Zhou, B. Hou, H.W. Zhang, M. Luo, Y.P. Li, Engineering nanoparticles to locally activate T cells in the tumor microenvironment, Sci. Immunol. 4 (2019) eaau6584.

[17] Y.F. Yin, X.W. Jiang, L.P. Sun, H.Y. Li, C.X. Su, Y. Zhang, G. Xu, X.L. Li, C.K. Zhao, Y. Chen, H.X. Xu, K. Zhang, Continuous inertial cavitation evokes massive ROS for reinforcing sonodynamic therapy and immunogenic cell death against breast carcinoma, Nano Today 36 (2021) 101009.

[18] A. Snyder, V. Makarov, T. Merghoub, J. Yuan, J.M. Zaretsky, A. Desrichard, L. A. Walsh, M.A. Postow, P. Wong, T.S. Ho, T.J. Hollmann, C. Bruggeman, K. Kannan, Y.Y. Li, C. Elipenahli, C.L. Liu, C.T. Harbison, L.S. Wang, A. Ribas, J. D. Wolchok, T.A. Chan, Genetic basis for clinical response to CTLA-4 blockade in melanoma, N. Engl. J. Med. 371 (2014) 2188–2199.

[19] J. Wang, J.W. Sun, L.N. Liu, D.B. Flies, X.X. Nie, M. Toki, J.P. Zhang, C. Song, M. Zarr, X. Zhou, X. Han, K.A. Archer, T. O'Neill, R.S. Herbst, A.N. Boto, M. F. Sanmamed, S. Langermann, D.L. Rimm, L.P. Chen, Siglec-15 as an immune suppressor and potential target for normalization cancer immunotherapy, Nat. Med. 25 (2019) 656–666.

[20] M. Molgora, E. Esaulova, W. Vermi, J.C. Hou, Y. Chen, J.Q. Luo, S. Brioschi, M. Bugatti, A.S. Omodei, B. Ricci, C. Fronick, S.K. Panda, Y. Takeuchi, M.M. Gubin, R. Faccio, M. Cella, S. Gilfillan, E.R. Unanue, M.N. Artyomov, R.D. Schreiber, M. Colonna, TREM2 modulation remodels the tumor myeloid landscape enhancing anti-PD-1 immunotherapy, Cell 182 (2020) 886–900.

[21] Q. Chen, C. Wang, X.D. Zhang, G.J. Chen, Q.Y. Hu, H.J. Li, J.Q. Wang, D. Wen, Y. Q. Zhang, Y.F. Lu, G. Yang, C. Jiang, J. Wang, G. Dotti, Z. Gu, In situ sprayed bioresponsive immunotherapeutic gel for post-surgical cancer treatment, Nat. Nanotechnol. 14 (2019) 89–97.

[22] R.T. Manguso, H.W. Pope, M.D. Zimmer, F.D. Brown, K.B. Yates, B.C. Miller, N. B. Collins, K. Bi, M.W. Lafleur, V.R. Juneja, S.A. Weiss, J. Lo, D.E. Fisher, D. Miao, E. Van Allen, D.E. Root, A.H. Sharpe, J.G. Doench, W.N. Haining, In vivo CRISPR screening identifies Ptpn2 as a cancer immunotherapy target, Nature 547 (2017) 413–418.

[23] T. Luo, D. Wang, L.D. Liu, Y. Zhang, C.Y. Han, Y. Xie, Y. Liu, J.C. Liang, G.H. Qiu, H.X. Li, D.K. Su, J.J. Liu, K. Zhang, Switching reactive oxygen species into reactive

nitrogen species by photocleaved O-2-Released nanoplatforms favors hypoxic tumor repression, Adv. Sci. 8 (2021) 2101065.
[24] M. Nishida, K. Watanabe, Y. Sato, M. Nakaya, N. Kitajima, T. Ide, R. Inoue, H. Kurose, Phosphorylation of TRPC6 channels at Thr69 is required for anti-hypertrophic effects of phosphodiesterase 5 inhibition, J. Biol. Chem. 285 (2010) 13244–13253.
[25] K. Zhang, Y. Cheng, W.W. Ren, L.P. Sun, C. Liu, D. Wang, L.H. Guo, H.X. Xu, Y. X. Zhao, Coordination-responsive longitudinal relaxation tuning as a versatile MRI sensing protocol for malignancy targets, Adv. Sci. 5 (2018) 1800021.
[26] J.Y. Zhu, D.W. Zheng, M.K. Zhang, W.Y. Yu, W.X. Qiu, J.J. Hu, J. Feng, X.Z. Zhang, Preferential cancer cell self-recognition and tumor self-targeting by coating nanoparticles with homotypic cancer cell membranes, Nano Lett. 16 (2016) 5895–5901.
[27] N. Nath, K. Kashfi, Tumor associated macrophages and ʾNO, Biochem. Pharmacol. 176 (2020) 113899.
[28] V.T. Cheriyan, M. Alfaidi, A.N. Jorgensen, M.A. Alam, C.S. Abdullah, G.K. Kolluru, S. Bhuiyan, C.G. Kevil, A.W. Orr, H.W. Nam, Neurogranin regulates eNOS function and endothelial activation, Redox Biol 34 (2020) 101487.
[29] K. Zhang, H.X. Xu, X.Q. Jia, Y. Chen, M. Ma, L.P. Sun, H.R. Chen, Ultrasound-triggered nitric oxide release platform based on energy transformation for targeted inhibition of pancreatic tumor, ACS Nano 10 (2016) 10816–10828.
[30] B. Dunkerly-Eyring, D.A. Kass, Myocardial phosphodiesterases and their role in cGMP regulation, J. Cardiovasc. Pharmacol. 75 (2020) 483–493.
[31] I.M. Grumbach, W. Chen, S.A. Mertens, D.G. Harrison, A negative feedback mechanism involving nitric oxide and nuclear factor kappa-B modulates endothelial nitric oxide synthase transcription, J. Mol. Cell. Cardiol. 39 (2005) 595–603.
[32] B. Musicki, U.A. Anele, J.D. Campbell, S. Karakus, S. Shiva, F.H. Silva, A.L. Burnett, Dysregulated NO/PDE5 signaling in the sickle cell mouse lower urinary tract: reversal by oral nitrate therapy, Life Sci. 238 (2019) 116922.
[33] S.H. Francis, J.L. Busch, J.D. Corbin, cGMP-dependent protein kinases and cGMP phosphodiesterases in nitric oxide and cGMP action, Pharmacol. Rev. 62 (2010) 525–563.
[34] S. Talarek, J. Listos, J. Orzelska-Gorka, M. Jakobczuk, J. Kotlinska, G. Biala, The importance of L-arginine:NO:cGMP pathway in tolerance to flunitrazepam in mice, Neurotox. Res. 31 (2017) 309–316.
[35] M.M. Cortese-Krott, E. Mergia, C.M. Kramer, W. Luckstadt, J. Yang, G. Wolff, C. Panknin, T. Bracht, B. Sitek, J. Pernow, J.P. Stasch, M. Feelisch, D. Koesling, M. Kelm, Identification of a soluble guanylate cyclase in RBCs: preserved activity in patients with coronary artery disease, Redox Biol 14 (2018) 328–337.
[36] K. Zhang, H.Y. Li, J.Y. Lang, X.T. Li, W.W. Yue, Y.F. Yin, D. Du, Y. Fang, H. Wu, Y. X. Zhao, C. Xu, Quantum yield-engineered biocompatible probes illuminate lung tumor based on viscosity confinement-mediated antiaggregation, Adv. Funct. Mater. 29 (2019) 1905124.
[37] J. Chen, H.L. Luo, Y. Liu, W. Zhang, H.X. Li, T. Luo, K. Zhang, Y.X. Zhao, J.J. Liu, Oxygen-self-produced nanoplatform for relieving hypoxia and breaking resistance to sonodynamic treatment of pancreatic cancer, ACS Nano 11 (2017) 12849–12862.
[38] Y. Zhang, Y.F. Yin, W. Zhang, H.Y. Li, T.X. Wang, H.H. Yin, L.P. Sun, C.X. Su, K. Zhang, H.X. Xu, Reactive oxygen species scavenging and inflammation mitigation enabled by biomimetic prussian blue analogues boycott atherosclerosis, J. Nanobiotechnol. 19 (2021) 161.
[39] K. Zhang, Y. Fang, Y.P. He, H.H. Yin, X. Guan, Y.Y. Pu, B.G. Zhou, W.W. Yue, W. W. Ren, D. Du, H.Y. Li, C. Liu, L.P. Sun, Y. Chen, H.X. Xu, Extravascular gelation shrinkage-derived internal stress enables tumor starvation therapy with suppressed metastasis and recurrence, Nat. Commun. 10 (2019) 5380.
[40] X. Guan, H.H. Yin, X.H. Xu, G. Xu, Y. Zhang, B.G. Zhou, W.W. Yue, C. Liu, L.P. Sun, H.X. Xu, K. Zhang, Tumor metabolism-engineered composite nanoplatforms potentiate sonodynamic therapy via reshaping tumor microenvironment and facilitating electron-hole pairs' separation, Adv. Funct. Mater. 30 (2020) 2000326.